energies

MDPI

Article

Simulation and Experimental Research on Arc-Induced Fires in Photovoltaic Systems

Runan Song [1,*], Penghe Zhang [1], Yang Xue [1] and Wei Wang [2]

[1] China Electric Power Research Institute, Beijing 100192, China; zhangpenghe@epri.sgcc.com.cn (P.Z.); xueyang3@epri.sgcc.com.cn (Y.X.)
[2] School of Electrical and Electronic Engineering, Shandong University of Technology, Zibo 255000, China; wwsdut@163.com
* Correspondence: runan_song@163.com

Abstract

DC fault arcs comprise one of the most serious safety hazards in photovoltaic systems, and their danger far exceeds that of AC arcs. DC arcs lack a natural zero-crossing point, and their burning time can last from several seconds to several minutes, which is sufficient to ignite cable lines and surrounding combustibles, causing fires. To explore the characteristics and mechanism of the ignition of external combustibles by DC fault arcs, this paper, based on the theory of magnetohydrodynamics (MHD), constructed a three-dimensional numerical simulation model of a DC fault arc considering the coupling of electromagnetic, thermal, and flow fields. A DC fault arc experimental platform that can simulate the actual working conditions of photovoltaic systems was built to verify the accuracy of the model. Based on this, by integrating the complex pyrolysis model and the combustion reaction model, and selecting cotton fibers as the typical combustible indicator substances, as stipulated in the UL 1699 standard, a coupled simulation model for the ignition of solid combustibles by direct current fault arcs was established. The numerical simulation of the entire ignition process of the arc was realized, and the coupling mechanism of heat transfer, mass transfer, and chemical reactions during the ignition process was revealed. The research results of this paper fill a research gap in the numerical simulation of arc ignition caused by DC faults in photovoltaic systems, clarify the fire ignition risk patterns of DC fault arcs under different working conditions, and provide important theoretical support and technical references for the formulation of arc fire prevention strategies and the optimized design of fault arc protection devices for photovoltaic systems and other DC power systems.

Keywords: fault arc; photovoltaic system; magnetohydrodynamics; combustion reaction; complex pyrolysis

Check for updates

Academic Editor: Carlo Renno

Received: 17 January 2026
Revised: 22 March 2026
Accepted: 28 March 2026
Published: 21 April 2026

Copyright: © 2026 by the authors. Licensee MDPI, Basel, Switzerland. This article is an open access article distributed under the terms and conditions of the Creative Commons Attribution (CC BY) license.

1. Introduction

Cable joint oxidation, insulation damage, poor contact, and other issues may cause DC fault arcs in photovoltaic systems [1]. Owing to the absence of natural zero-crossing points, DC fault arcs are difficult to extinguish naturally, and the temperature can exceed 3000 K, easily igniting the backplane of the component or surrounding combustible substances [2,3]. According to IEC international standards, about 60% of fires are related to the failure to cut off DC arcs in time [4]. Therefore, it is of great significance to study the electromagnetic thermal dynamic evolution of DC fault arcs and then to analyze the ignition characteristics of DC fault arcs for fire prevention strategies and to improve the safety management of PV systems.

At present, the main methods to study fault arc characteristics are experimental methods and simulation methods. Experimental methods can directly obtain the voltage and current characteristics of the arc. Aditya Shekhar, Liwei Du et al. developed an arc fault test and analysis platform based on UL 1699 [5] and GB 3143-1982 [6]. The platform includes an arc-generating device, cable-carbonizing device, and cable-cutting device. Arc can be generated under various fault conditions, such as terminal loosening, cable carbonization, and metal short circuit [4,7]. Jinru Huang et al. designed a series of fault arc waveform-generating devices. Based on the fault arc waveform database, the hardware circuit of a waveform recovery device was designed to generate arc current waveforms under specific fault types and loads [8]. However, it is difficult to analyze the complex physical phenomena of arcs using experimental methods, so it is necessary to conduct more in-depth research using numerical simulation methods.

Arc models are mainly divided into mathematical models based on centralized parameters and multi-physics models. Mathematical models based on centralized parameters include models based on static volt-ampere characteristics [9,10] and black box models represented by the Cassie model and Mayr model [11–14]. These types of models mainly focus on the volt-ampere characteristics of the arc and cannot reflect physical fields, such as heat and electricity, during the arc process. In addition, parameters such as time constants and power consumption are difficult to determine accurately, which further affects the accuracy of models. The representative arc multi-physical field coupling model is a model based on magnetohydrodynamics (MHD) theory. The MHD theory regards the arc plasma as a conducting high-temperature fluid and describes the interaction among the electromagnetic field, thermal field, and flow by solving fluid dynamics equations and electromagnetic field equations. Related research mainly focuses on scenarios such as switchgear opening and arc welding. Wang Q et al. simulated the arc extinction characteristics of a low-voltage circuit breaker based on the MHD method and considered the process of grid-cutting arcs [15]. Wen Wang et al. developed a plasma jet-triggered gas switch (PJT-GS) for a UHV DC transmission system. Based on the method of MHD, a three-dimensional arc model was established to analyze the influence of arc dynamic characteristics on operating performance [16]. Ali Kadivar et al. studied the high-speed stretching effect of arcs in ultra-high-speed switches [17]. Kai Bo, Zhenwei Ren, Keyao Huang et al. also applied MHD theory to low-voltage appliances, including contactors and MCBS, and simulated the motion of the arc plasma in the arc-breaking chamber in the process of contact separation, considering the electromagnetic force, temperature, and flow velocity characteristics. The effects of arc-extinguishing gas, magnetic field, and gas-forming material on arc-extinguishing effect have been analyzed [18–21]. Yeon Je Shin and Fenggui Lu et al. applied MHD theory to the study of arc welding, considered the thermal characteristics of the arc, the heat transfer of metal materials, and interaction between the arc and the melting pool, and analyzed the influence of atmosphere, metal steam, magnetic field, welding materials, and other factors on the welding effect [22–26]. Zhenhua Xie established a DC arc model of a PV system based on magnetic fluid and analyzed the heat transfer characteristics of the DC arc. However, the ignition process caused by electric arcs has not been further studied [27]. The above studies only focus on the characteristics of the arc, and there is a lack of research on the external environment affected by the arc.

Faults in power systems comprise an important factor that causes power system fires. Liang Zhou and Wenyue Wei designed experiments to generate AC arcs through arc-generating devices and studied the thermal behavior of electrodes and the ignition characteristics of printing paper under a 220 V AC arc fault with different currents [28]. Jing Zhang et al. established a finite element model of heat transfer for the high temperature caused by bad electrical contact and carried out experiments on the heat damage of the

insulation layer caused by high-temperature contact [29]. Xin Zhang used a wind tunnel and adopted the smog-helium similarity and scaling law to study the smoke diffusion of rooftop photovoltaic fires, proposing a fire prevention scheme for rooftop photovoltaic arrays [30]. Courty and Gong et al. established a numerical model of cable combustion under the action of an external heat source based on fire dynamics and studied its heat release rate, mass loss, and expansion behavior [31,32]. There are few studies on the ignition of combustibles by DC fault arcs. Numerical simulations of arc-induced fires have the following difficulties: (1) there is a complex multi-physical field coupling relationship in the evolution process of the arc; (2) as a kind of ignition source, DC arcs are highly nonlinear, making them difficult to represent by setting a constant fire source or a t^2 fire source in traditional fire simulations; and (3) the combustion of solid combustibles undergoes a complex chemical reaction process, and establishing a reasonable pyrolysis and combustion model is difficult.

This study focuses on the photovoltaic system. First, based on the theory of magnetohydrodynamics, a three-dimensional numerical model of a DC fault arc was constructed to investigate its evolution process and the spatial temperature distribution pattern. Subsequently, by combining the complex pyrolysis theory and combustion reaction theory, a three-dimensional simulation model for the ignition of solid combustibles by direct current fault arcs was established. The dynamic changes in key parameters such as heat release rate, temperature, and product composition during the arc ignition process were analyzed. Based on this, a comprehensive study on the risk patterns of arc-induced fires was conducted under different operating conditions of the photovoltaic system, and the mechanisms by which various key factors affect the ignition characteristics of the arc were analyzed. The research results can provide theoretical support for fire prevention and disaster reduction in power systems and have significant practical engineering significance for improving the safety management level of photovoltaic systems. The structure of this paper is as follows. In Section 2, the MHD theory of the arc is presented and the 3D simulation model of the DC arc is established. In Section 3, the theories of pyrolysis and combustion are presented, and the solid combustion simulation model is established based on these theories. In Section 4, an experimental platform is built to verify the effectiveness of the simulation model. On this basis, the process of the ignition of combustible by electric arcs is deeply analyzed. In addition, the ignition characteristics and fire risk of the arc under various operating conditions of the PV system are studied. Section 5 presents the conclusion.

2. Arc Plasma Model Based on MHD Theory

2.1. Governing Equations of MHD

For arc models, the MHD theory is a widely adopted method. Magnetohydrodynamics is based on the local thermodynamic equilibrium (LTE) assumption, which states that the arc column region is in a fully ionized state, and the thermodynamic quantities such as the temperature, pressure, and density of the plasma are uniform and satisfy the thermodynamic equilibrium relationship. For the stable arc ignition process, refs. [15–27] all demonstrated the effectiveness of magnetohydrodynamics in arc ignition simulation. The arc extinction and post-arc process are in a non-local thermodynamic equilibrium state. Considering that the research object of this paper is a direct current arc, which is different from an alternating current arc, there is no periodic extinction and re-ignition. This will also be mentioned in Section 4.1. In this paper, the arc is extinguished by cutting off the external power supply, so there is no problem of arc re-ignition. Therefore, this paper selects the magnetohydrodynamic method to establish an arc model. At the same time, considering that there are no large external gas flows or arc blowing in the experimental environment

of this paper, and referring to the setting of similar arc conditions in ref. [33] and other literature, this paper assumes that the flow pattern of the arc is laminar. To reduce the complexity of the simulation and improve the stability of the model, the erosion of the arc on the electrode and the influence of material phase change on the arc are ignored.

The fluid characteristics of arc plasma are governed by the mass conservation equation, momentum conservation equation, and energy conservation equation:

$$\frac{\partial \rho}{\partial t} + \nabla \cdot (\rho \boldsymbol{u}) = 0 \tag{1}$$

$$\frac{\partial (\rho T)}{\partial t} + \nabla \cdot (\rho \boldsymbol{u} T) = \nabla \cdot (\frac{\lambda}{c_p} \nabla T) + \boldsymbol{J} \cdot \boldsymbol{E} - S_{rad} \tag{2}$$

$$\frac{\partial (\rho \boldsymbol{u}_i)}{\partial t} + \nabla \cdot (\rho u_i \boldsymbol{u}) = \nabla \cdot (\mu \nabla u_i) - \nabla p + \boldsymbol{J} \times \boldsymbol{B} \tag{3}$$

In the equations, t represents time, ρ represents density, $\boldsymbol{u}$ represents a velocity vector, c_p represents specific heat, T represents temperature, λ represents thermal conductivity, $\boldsymbol{J}\cdot\boldsymbol{E}$ represents Joule heat, $\boldsymbol{J}$ represents current density, $\boldsymbol{E}$ represents electric field strength, S_{rad} represents radiant energy, p represents pressure, and $\boldsymbol{B}$ represents magnetic flux density.

Radiation energy is determined by the following equation:

$$q_{rad} = 4\alpha k (T^4 - T_0^4) \tag{4}$$

In the equation, α represents the Stefan–Boltzmann constant, and its value is 5.67×10^{-8} W/(m^{2}K^4); k represents an absorption coefficient; and T_0 represents environmental temperature.

The characteristics of electromagnetic fields are described by the Maxwell–Ampère equations:

$$\nabla \cdot (-\sigma \nabla \varphi) = 0 \tag{5}$$

$$\boldsymbol{E} = -\nabla \varphi \tag{6}$$

$$\boldsymbol{J} = \sigma \boldsymbol{E} \tag{7}$$

In the equations, σ represents electrical conductivity, and φ represents electric potential.

2.2. Geometric Model and Boundary Conditions of DC Arc

The arc is located in the electrode gap. To enhance computational efficiency, a geometric model is constructed focusing on the vicinity of the electrode gap. As illustrated in Figure 1a, the three-dimensional geometric model comprises a copper electrode, a graphite electrode, and the surrounding air domain. The ambient temperature is set to 300 K, with an initial environmental pressure of 1.01×10^5 Pa. The fluid dynamics software Fluent 17.2 was used for secondary development. The fluid dynamics equations were solved using Fluent, and user-defined functions were utilized to load electromagnetic field parameters such as current density and Joule heat. Figure 1b shows the mesh division (section) of the arc model. The mesh division method adopts the hexahedral dominant method, and a total of 499,481 elements are included. For the main electrode gap area where the arc column mainly exists, denser elements with a size of 0.05 mm are used, while larger-sized elements are used for the areas far from the arc column. The simulation uses the SIMPLE transient solver and employs the second-order upwind scheme. The simulation duration is 2.5 s, the simulation step size is 1×10^{-4} s, and the maximum number of iterations for each time step is 2000. All other solution settings are set according to the default settings of the software.

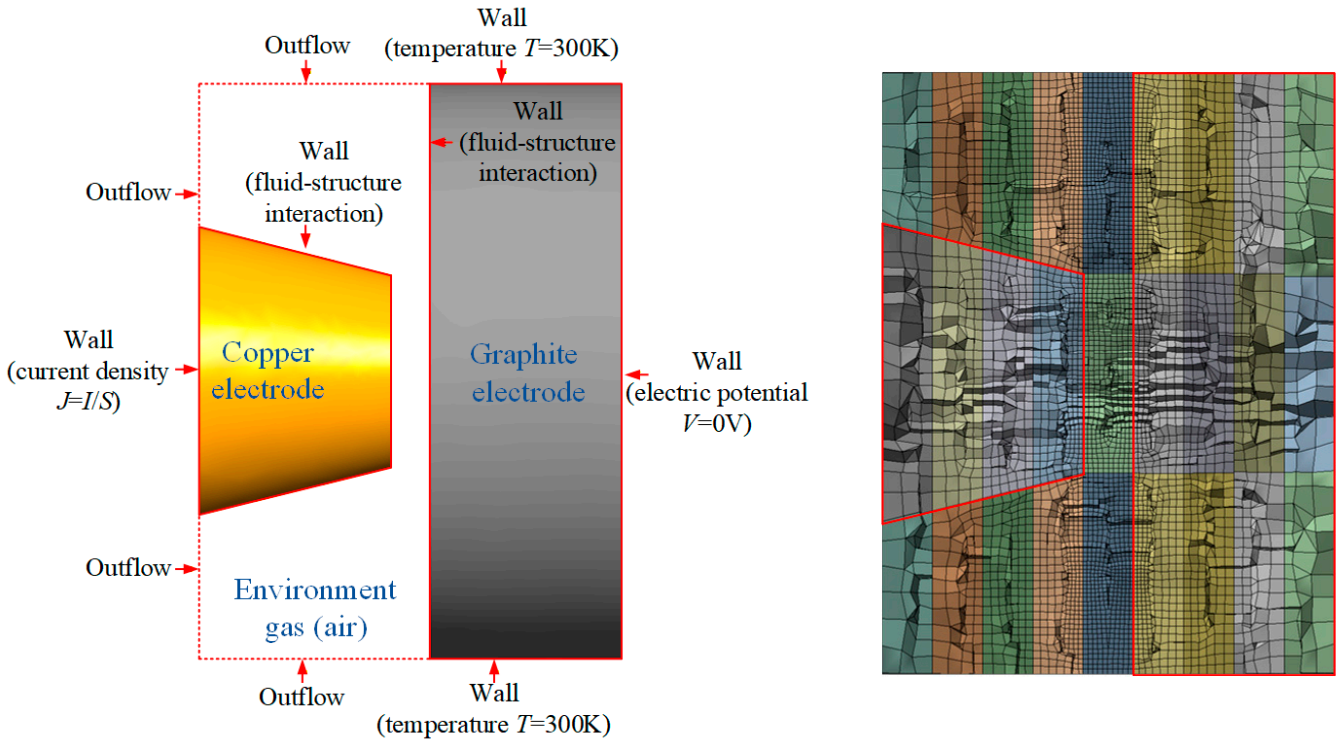


Figure 1. DC arc model: (**a**) geometric model; (**b**) meshing.

The heat of the arc is primarily conducted through the contact surface of the electrodes and dissipated into the surrounding gas medium via thermal convection. The boundary of the fluid domain is set as the outflow boundary, and the fluid–solid interface is set as a coupled wall boundary, with continuous temperature and heat flux density across the interface:

$$q_{ae} = -\lambda_a \frac{\partial T}{\partial z} \tag{8}$$

$$q_{ea} = -\lambda_e \frac{\partial T}{\partial z} \tag{9}$$

$$T_{sw} = T_{fw} \tag{10}$$

$$q_{sw} = q_{fw} \tag{11}$$

In the equations, q_{ae} represents the heat flux density conducted by the arc to the electrode; q_{ea} represents the heat flux density transmitted by the electrode to the arc; λ_a represents the thermal conductivity of the arc medium; λ_e represents the thermal conductivity of the electrode materials; T_{sw} and T_{fw} represent the temperatures of the solid wall and the fluid wall at the fluid–solid interface, respectively; and q_{sw} and q_{fw} represent the heat flux densities of the solid wall and the fluid wall at the fluid–solid interface, respectively.

As shown in Figure 1, the left surface of the copper electrode is configured with a current density distribution as specified in Equation (12), while the right surface of the graphite electrode is set to zero electrical potential:

$$J = I/S \tag{12}$$

In the equation, J represents the current density distributed over the surface of the copper electrode, I represents the current value, and S represents the area that current flows through.

3. Combustion Reaction Model Based on Complex Pyrolysis Model

3.1. Governing Equations of Combustion Model

The flow in a fire is low Mach number compressible flow and is generally described by the N-S viscous fluid equation for low-speed flow. In addition, the combustion essence of the flame is an oxidation reaction, which needs to satisfy the component conservation equation and thermodynamic state equation in chemical reactions, as shown below:

$$\frac{\partial \rho}{\partial t} + \nabla \cdot (\rho \boldsymbol{u}) = \dot{m}_b''' \tag{13}$$

$$\frac{\partial (\rho h)}{\partial t} + \nabla \cdot (\rho h \boldsymbol{u}) = \frac{Dp}{Dt} + \dot{q}''' + \dot{q}_b''' - \nabla \cdot \dot{q}'' \tag{14}$$

$$\rho(\frac{\partial \boldsymbol{u}}{\partial t} + (\boldsymbol{u} \cdot \nabla)\boldsymbol{u}) + \nabla p = \rho g + \nabla \cdot \tau \tag{15}$$

$$\frac{\partial (\rho Y_i)}{\partial t} + \nabla \cdot (\rho Y_i \boldsymbol{u}) = \nabla \cdot (\rho D_i \nabla Y_i) + \dot{m}_i''' \tag{16}$$

In the equations, $\dot{m}_b$ represents the gaseous components increased by pyrolysis or evaporation; $\dot{q}'''$ represents the heat released per unit volume in a chemical reaction; $\dot{q}_b{}'''$ represents the energy changes caused by sub-grid scale particles such as droplets and particles; $\dot{q}''$ represents the conduction, convection, and radiation heat transfer; g represents gravitational acceleration; τ represents a viscous stress tensor; Y_i represents the mass fraction of component I; and $\dot{m}_i{}'''$ represents the generation or dissipation rate of component i per unit volume.

The combustion of solid materials is a complex physicochemical process. When solid materials are heated, they first undergo pyrolysis reactions, generating flammable volatile products such as hydrocarbons, hydrogen, and carbon monoxide, as well as non-flammable volatile products. After the flammable volatile products escape, they mix with oxygen to form flammable gas mixtures, providing fuel for subsequent combustion reactions. The flammable gases react with oxygen in oxidation reactions, releasing a large amount of heat and sustaining the combustion. The heat conduction and heat transfer of solid combustibles are expressed as follows:

$$\rho c \frac{\partial T}{\partial t} = \frac{\partial}{\partial x}(k \frac{\partial T}{\partial x}) + \dot{q}''' + \dot{q}'' \tag{17}$$

In the pyrolysis model of solid combustibles, the reaction rate of the i-th component can be expressed by the Arrhenius equation:

$$r_i = (\frac{\rho_{s,i}}{\rho_{s0}})^{n_s} A_i \exp(-\frac{E_i}{RT_s}) \tag{18}$$

In the equations, $\rho_{s,i}$ represents the solid density during the reaction process, ρ_0 represents the initial solid density, A_i represents a pre-exponential factor, E_i represents the activation energy, and T_s represents the reaction temperature.

The combustion reaction is a complex process. Pyrolysis generates a wide variety of combustible gases, which undergo multiple chemical reactions with oxygen in the air. The resulting products are characterized by multiple states and large quantities. From the perspective of chemical kinetics, a simple combustion reaction equation may consist of hundreds or even thousands of elementary reactions. Solving the mass transport equation for all gas species during the simulation process will significantly increase the computational

cost and may lead to non-convergence of the calculation. To simplify the simulation process and avoid the calculation of complex chemical reactions, a mixed control combustion model is adopted. The model divides the reaction into three parts, fuel, air, and products, to describe the turbulent combustion of gaseous fuel and oxygen. Each part is treated as a 'lumped species' and, in the simulation, each lumped species is regarded as a whole for solution, as shown below:

$$\begin{aligned} &C_xH_yO_zX_n + v_{O_2}(O_2 + 3.76N_2) \rightarrow \\ &\nu_{CO_2}CO_2 + v_{H_2O}H_2O + v_{CO}CO + v_sSoot + v_{N_2}N_2 + nX \end{aligned} \tag{19}$$

In the equations, X represents the other elements in the chemical formula besides carbon, hydrogen, and oxygen.

The relationships among the values of the stoichiometric coefficients in the above formula are expressed as follows:

$$x = v_{CO_2} + v_{CO} + v_S \tag{20}$$

$$y = 2v_{H_2O} \tag{21}$$

$$z + 2v_{O_2} = 2v_{CO_2} + v_{H_2O} + v_{CO} \tag{22}$$

$$v_{N_2} = 3.76v_{O_2} \tag{23}$$

According to the UL 1699 standard, cotton fiber material is selected as the standard combustion indicator. Cotton fiber material is a relatively flammable fuel that is widely present in residences, making it a substitute for complex fuels and capable of revealing the arc fault ignition capability.

This paper assumes that the cotton fibers are pure and that the pyrolysis gases react completely with oxygen. The chemical reactions are single-step reactions, that is, the pyrolysis gases react with oxygen in one step to produce the final products without going through intermediate chemical reactions. The chemical formula of the combustible volatile gas produced by the pyrolysis of cotton fiber material can be written as $C_6H_{10}O_5$, and its combustion chemical reaction equation is as follows:

$$C_6H_{10}O_5 + 6(O_2 + 3.76N_2) \rightarrow 6CO_2 + 5H_2O + 22.56N_2 \tag{24}$$

3.2. Geometric Model and Boundary Conditions

A numerical simulation model for the arc-induced combustion was established based on the fire dynamics software FDS 6.5 (Fire Dynamics Simulator). The geometric model of the simulation is shown in Figure 2. The three-dimensional geometric model includes copper electrodes, graphite electrodes, the background gas domain, and combustibles. Among them, the geometry of the combustibles is set as a cube of 10 mm × 10 mm × 10 mm. The bottom surface of the calculation domain is set as an inert boundary, and the four sides and top surface are set as open boundaries. The background gas of the calculation domain is set as air (consisting of 21% O_2 and 79% N_2). The effect of the arc heat source is reflected through the heater. Two monitoring points are set at 0.5 mm and 2.0 mm below the lower surface of the combustible material, and four monitoring points are set at 0.5 mm, 5.0 mm, 10.0 mm, and 15.0 mm above the upper surface. Thermocouples and gas detectors are placed at the monitoring points to obtain the changes in flame temperature and pyrolysis gas and combustion products.

The combustion of combustible materials depends on the heat provided by the thermal environment around the fuel. In combustion simulations, the ignition of combustible materials is achieved by setting the location and power of the fire source. In the fire

dynamics software FDS, a heat source can be simulated by setting the HRRPUA (heat release rate per unit area) of the burner boundary or the net heat flux of the heater boundary. The burner boundary is generally used to simulate a flame with a definite heat release rate or mass consumption rate, while the heater boundary simulates a radiant heat source.

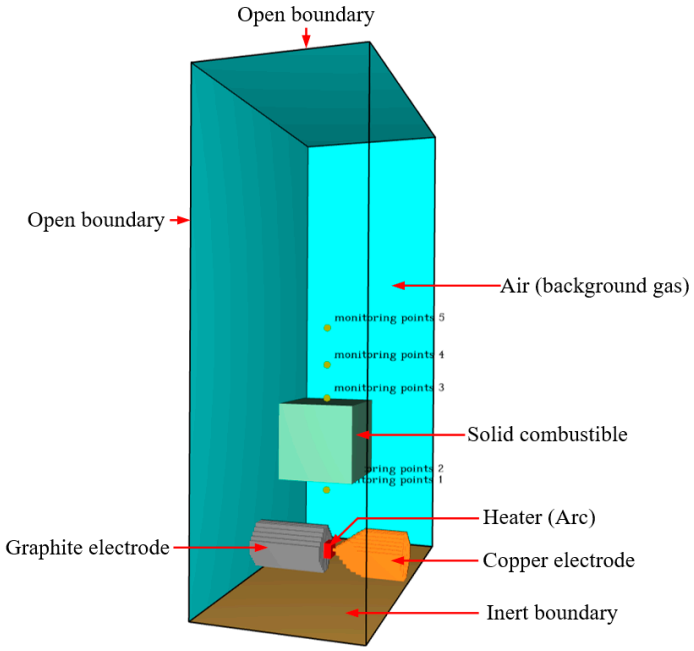


Figure 2. Combustion geometric model.

HRRPUA requires the use of a cone calorimeter to test and obtain the heat release rate curve per unit area of the material. Due to the high temperature and other characteristics of the electric arc, it is difficult to directly measure its HRRPUA. Therefore, in this paper, the net heat flux per unit area on the surface of the heater is calculated based on the MHD arc model results at each moment and loaded into the combustion model as the heat flux per unit area of the arc plasma in the electrode boundary region.

In the combustion model, the arc is regarded as a heating element that continuously releases heat to the external environment during the arcing process. As can be seen from the above description of the heat source setting in FDS, the heat source in FDS is generally considered to emit heat flux outward from a certain surface. The arc can be approximately regarded as a cylinder with radius r [34]. In most cases, the arc image presents a bright central region (i.e., the arc column) and a wider outer region with lower brightness (i.e., the aperture). The diameter of the bright central part of the arc is roughly equivalent to that of the arc column. This region serves as the main conductive channel of the arc, through which almost 100% of the current flows, and it is also the main heat-generating area of the arc. The outer region is mainly formed by the heat diffused from the core heat-generating area of the arc through heat conduction, heat convection, heat radiation and other effects. Therefore, the region through which the current mainly flows can be equivalent to a heating element, as shown in Figure 3.

To equivalently represent the effect of the arc in the combustion model, it is necessary to define the heat-generating boundary surface of the arc, that is, to calculate the radius r of the arc column. On this basis, the time-varying heat flux on the heat-generating surface of the arc is obtained and applied as the load of the heat source in FDS. In the environment studied in this paper, there are no strong convection or other heat dissipation measures. The heat source for the stable combustion of the arc is mainly composed of the Joule heat

generated by the current and the power loss caused by radiation and other factors. The heat flux of the arc heating element can be calculated using Equation (25):

$$q_h = \frac{\int_{\Omega} (P_j - P_d) dV}{2\pi r l} \tag{25}$$

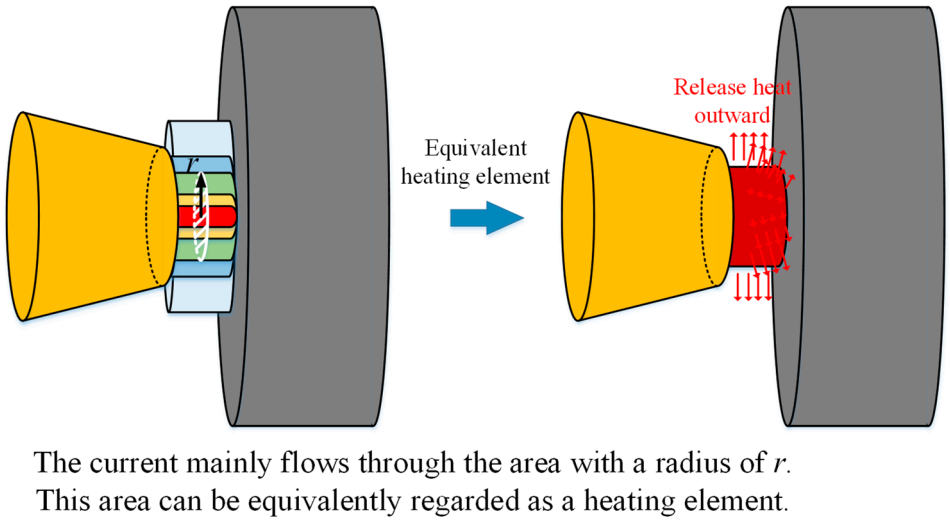


Figure 3. Equivalent representation of an arc as a heating element.

In the equation, P_j represents the Joule power, P_d represents the power loss, r represents the radius of the arc column, l represents the electrode gap distance, dV represents the volume of a cell in Fluent, and Ω represents the arc column region.

Under the research conditions of this paper, the distance between combustibles and the arc is relatively large, and the arc duration is short. Therefore, the temperature generated by cotton combustion does not directly act on the core region of the arc and has limited influence on the arc. In addition, since there is no direct coupling interface between Fluent and FDS, a unidirectional parameter transfer method is adopted in this paper.

A process control module is developed using C# to automatically control data transfer between the arc model and the combustion model, as shown in Figure 4.

1. First, the process control module launches Fluent and activates the DC arc simulation module.
2. In the DC arc simulation module, simulation parameters including materials, source terms, and boundary conditions are set according to Sections 2.1 and 2.2. The user-defined functions are compiled and linked, and the dynamic link library is imported, then the solution starts.
3. After the solution of each time step of the arc is completed, the arc column radius, Joule power, and dissipation power are calculated using UDF. For the arc radius, a circular section with an initial radius $r = r_0$ is assumed at the arc center, and the current density in this section is integrated. The calculated current I_c is compared with the total arc current I. If $|I - I_c| < \varepsilon$ is satisfied, r is determined as the arc radius; otherwise, let $r = r_0 + \Delta r$ and repeat the above steps until I_c approaches the arc current I. The Joule power and dissipation power correspond to the last two terms of Equation (2). The radius and power parameters are exported to the results file, respectively.
4. After the DC arc simulation is finished, a termination flag file of the DC arc solution is output through UDF. When the process control module detects the flag file, it reads the DC arc simulation results and calculates the arc heat flux of the DC arc result at each moment according to Equation (25).

5. FDS enables programmatic modeling and full-process control of fire scenarios through scripts. After obtaining the time-varying heat flux values, a console program is used to generate scripts for FDS modeling and heat source setup, and batch commands are invoked to launch the solution of the combustion module. FDS employs a variable step size algorithm. The solver automatically performs an interpolation on the heat flux based on the current solving time.

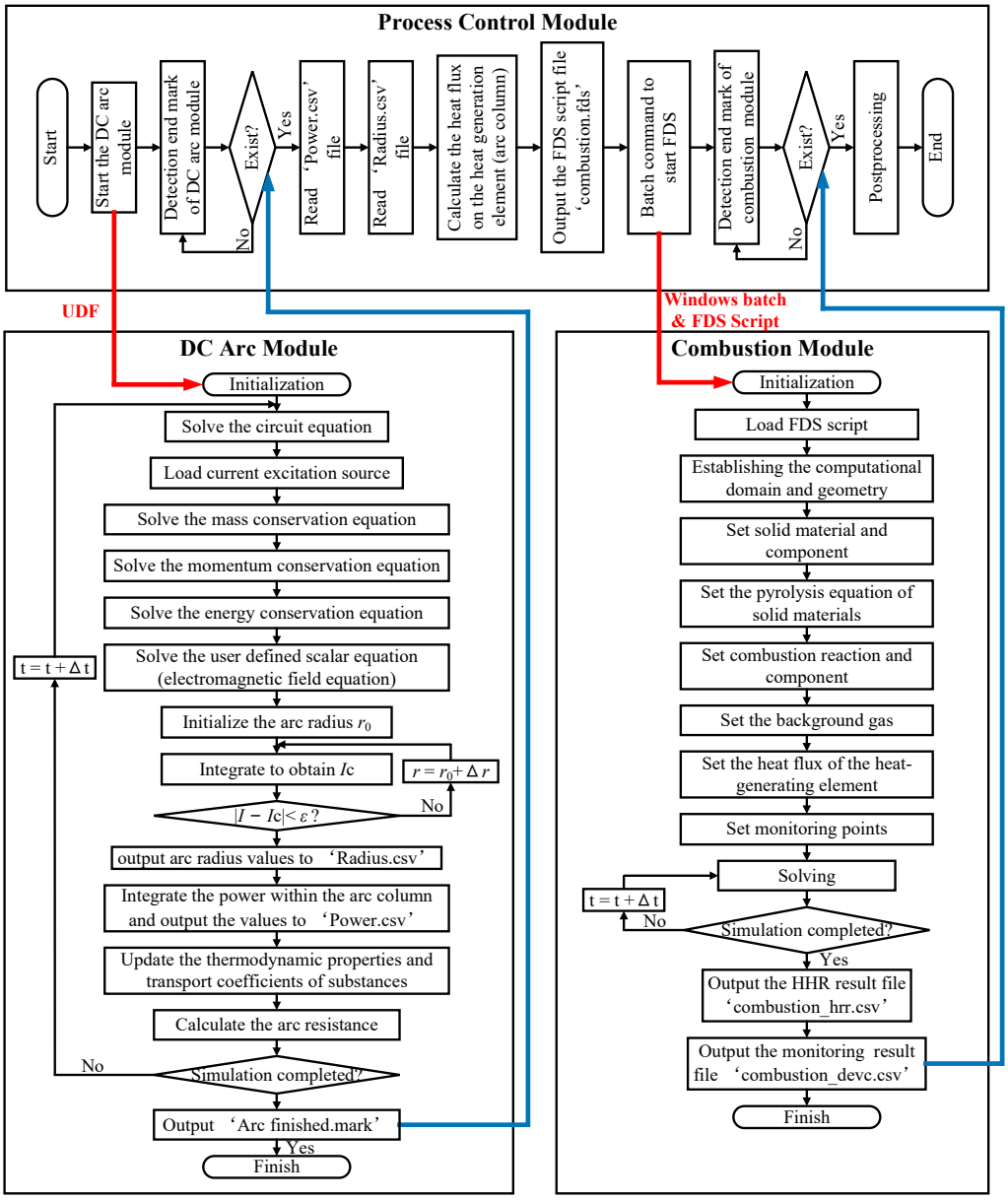


Figure 4. Solution flowchart.

4. Results and Analysis

4.1. Experimental Verification

As shown in Figure 5, the DC fault arc experiment platform mainly consists of a photovoltaic array, an energy storage simulation source, a fault arc-generating device, a line impedance network, a resistive load, an inverter, line cables, and a protection switch. This experimental platform can simulate various scenarios of a photovoltaic system, including normal operation, inverter startup process, shading, different irradiance levels, and energy storage battery simulation charging and discharging. The fault arc-generating device

adopts the arc-generating method of arc pulling. After opening the copper electrode and graphite electrode using a stepper motor, the arc is generated at the moment of separation. This device is capable of generating arc faults in circuits caused by factors such as broken wires, loose connection terminals, and poor contact.

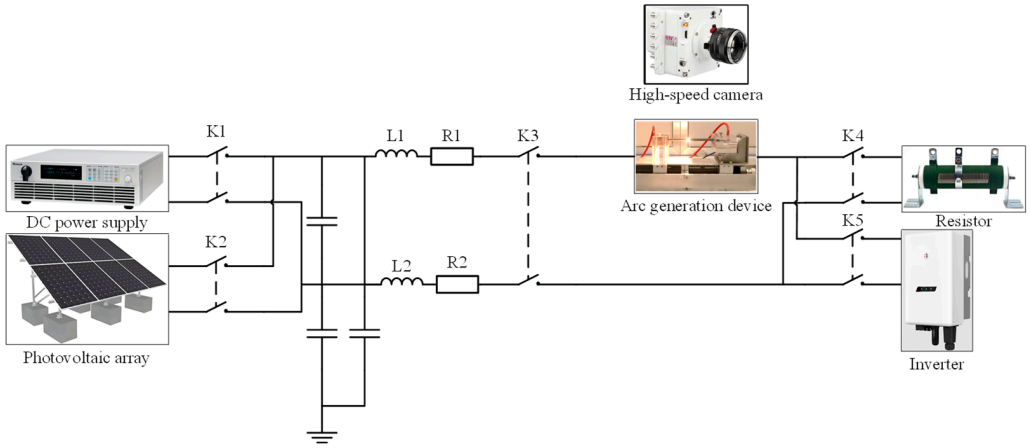


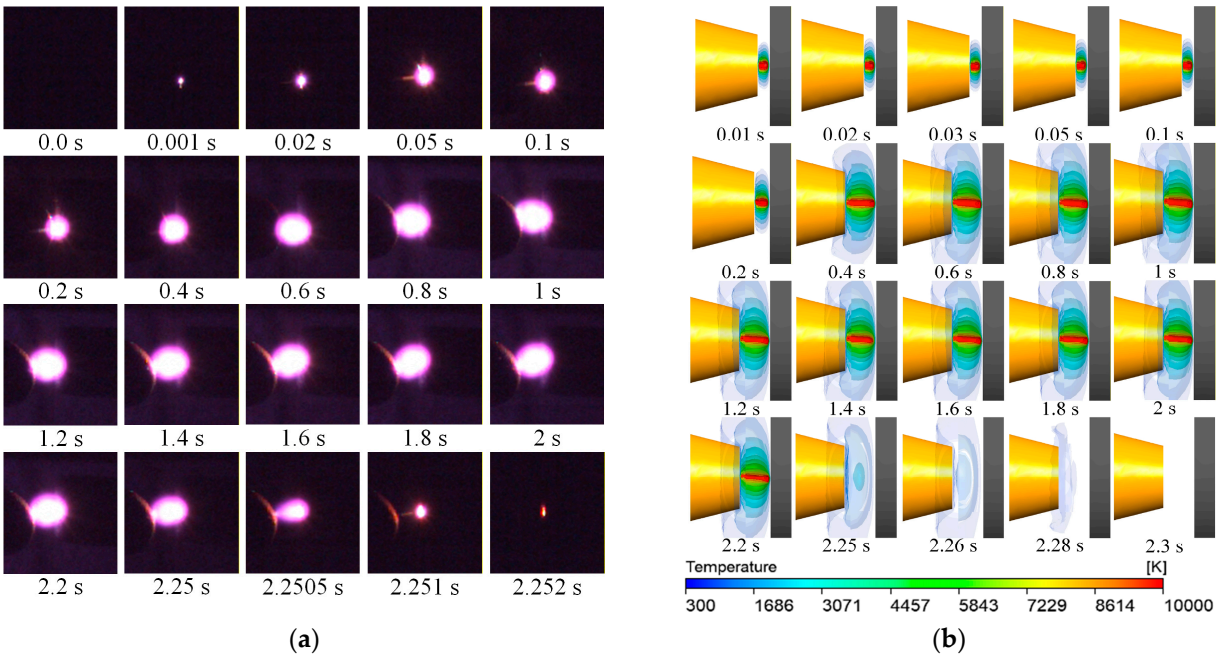
Figure 5. DC fault arc experimental platform.

During the experiment, the state of the arc is manifested in two aspects: the intensity variation of the arc light and the stability of the arc voltage and current waveforms. Figure 6a shows images of the arc's morphological changes captured by a high-speed camera. As shown in the figure, as the electrodes separate, the arc appears in the middle of the electrodes. At 0.001 s, a faint light spot appears between the edge of the copper electrode and the graphite electrode, indicating that a discharge occurs in the electrode gap and the arc is generated. However, due to the small electrode gap, the arc is not obvious. As time progresses, the discharge channel widens, and the area of the arc gradually expands. After 0.01 s, it gradually evolves into a distinct light mass. Subsequently, as the electrode gap increases, the brightness and area of the arc continue to increase. After 0.6 s, when the electrode distance reaches approximately 1.0 mm, the stepping motor stops working, and the electrode gap remains at around 1.0 mm. Thereafter, the length and brightness of the arc remain stable, entering a stable stage. At 2.25 s, the power supply is cut off, and the brightness of the arc gradually dims, its area decreases, and the arc extinguishes rapidly. At 2.251 s, there is no continuous arc channel in the electrode gap.

Figure 6b shows the development of the arc temperature distribution obtained through simulation. As shown in the figure, the highest temperature of the arc is located in the arc column region in the center, where the temperature exceeds 10,000 K. The temperature on the outer side of the arc is lower but still reaches thousands of Kelvin. With an increase in the electrode distance, the temperature of the arc gradually diffuses outward, which is an important cause of fires. By comparing it with the arc images captured by a high-speed camera, it can be seen that the development trend of the arc in the simulation is basically consistent with that in the experiment.

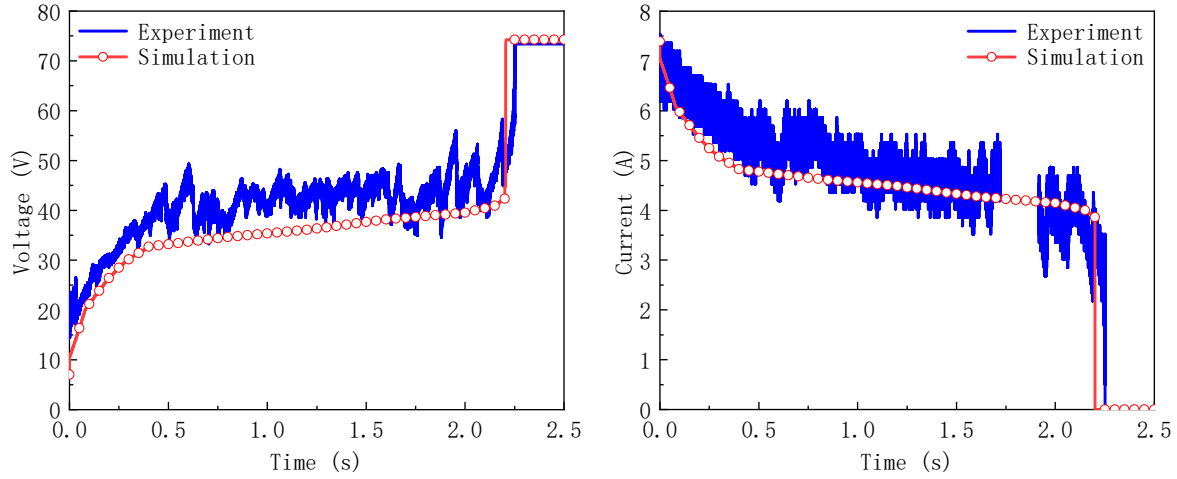
Figure 7a shows the arc voltage obtained from the experiment and simulation, and Figure 7b shows the arc current curves from the experiment and simulation. As shown in the figure, before 0.0007 s, the arc voltage rises rapidly and the arc current drops rapidly. This is because the electrode separation process elongates the arc, increasing the arc resistance and causing the arc voltage to rise and the arc current to fall. When the electrode distance stabilizes, the arc voltage and current remain basically stable. Due to the expansion of the arc volume, convective heat transfer with the external environment, and heat conduction through the electrodes, the arc voltage slowly rises and the current slowly drops. After the

power supply is cut off, the arc loses its energy source and the current rapidly drops to zero. By comparing the simulation and experimental curves, it can be seen that the trends of the arc voltage and current curves obtained from the simulation are basically consistent with those from the experiment. The arc voltage obtained from the simulation is slightly lower than that from the experiment, and the rate of current decline during the electrode elongation stage in the simulation is slightly faster than that in the experiment. The possible reasons for this are that the simulation sets the electrode movement speed as a constant 2.5 mm/s, but in the experiment, due to factors such as stepper motor control, the actual arc elongation speed may be different, and there may also be errors in the electrode holding distance. In addition, the model in this paper does not consider the sheath influence of the metal vapor produced by arc erosion of the electrodes, which may also cause errors.



(**a**) (**b**)

Figure 6. The evolution process of an electric arc: (**a**) experiment; (**b**) simulation.



(**a**) (**b**)

Figure 7. Comparison of simulation and experiment: (**a**) arc voltage; (**b**) arc current.

4.2. Discussion of Model Applicability

In establishing the arc model, to balance computational accuracy and solution complexity, this paper adopts the assumptions of LTE state, laminar flow field, and neglecting electrode ablation. A brief discussion on the applicable scope of each assumption and its potential influence on the simulation results is presented below to clarify the physical boundaries and limitations of the model.

The LTE assumption is applicable to the high-temperature core region of the arc. In the plasma sheath and the weakly ionized region near the electrodes, delayed energy exchange between electrons and heavy particles may lead to a slightly lower calculated temperature in the sheath region than the actual physical value. Moreover, neglecting the sheath effect results in a slightly lower simulated arc voltage than the measured value. The arc sheath is located at the interface between the electrode and the arc column, and it has limited influence on heat transfer from the arc to the surrounding air. Under short-duration arcing conditions, electrode ablation is also limited. Therefore, since this study focuses on the heat flux output of the arc core and the overall ignition characteristics rather than the detailed sheath physics, the LTE assumption has limited impact on the calculation of the overall temperature and heat flux.

As for the selection of the flow field model, this paper adopts a laminar flow regime instead of a turbulence model, mainly based on the actual working conditions in the experimental environment without forced airflow or strong external disturbances. This assumption effectively reduces the computational cost and the risk of numerical divergence in the three-dimensional simulation. However, in practical engineering applications, if there is strong ventilation or air blowing on the arc, the coupling behavior between the arc and the surrounding fluid may exhibit turbulence characteristics. In such cases, the laminar assumption may underestimate the mixing rate and heat transfer efficiency. Therefore, the conclusions of this paper are mainly applicable to static, low-disturbance fault arc scenarios. For arc behavior in dynamic airflow environments, further research can be carried out by introducing turbulence models such as the k–ε model.

The paper does not consider the melting, evaporation, and vapor diffusion of copper electrodes caused by high-temperature arcs. In practice, electrode ablation consumes part of the arc energy and may produce metal vapor. The mixing of metal vapor and air changes local electrical conductivity and heat loss. This simplification may lead to a slight underestimation of arc energy loss and thus a slightly overestimated heat flux. Although the phase change of metal materials caused by high arc temperature is not directly considered, this paper still provides valuable references by analyzing the influence of copper vapor uniformly mixed with air at different concentrations on arc heating and ignition in Section 4.7. In future work, a metal phase-change model and metal vapor transport equations will be introduced to further improve the model completeness.

In summary, despite the above simplifications, the arc model established in this study can simulate the key characteristics of fault arcs and their ignition within the scope of no strong airflow and short arcing time, providing reliable theoretical and data support for arc fire risk assessment of photovoltaic systems.

4.3. Arc-Inducing Characteristic

Figure 8 shows the process of arc ignition of cotton and the changes in temperature. The simulation conditions were set as follows: 16 A DC for 3 s, with the cotton 10 mm away from the center of the electrode gap. As shown in the figure, the entire process can be divided into four stages: arc heating, flame development, intense combustion, and combustion weakening. The first 3 s comprise the arc heating stage, during which the arc heats the lower surface of the cotton. Under the high temperature of the arc, the lower

surface of the cotton is ignited at 1 s. From 1 to 3 s, the flame gradually intensifies, and the temperature of the lower surface of the cotton exceeds 1200 K. There is a connected high-temperature area between the electrode gap and the cotton, and the flame develops upward along the side. After 3 s, the arc extinguishes, and the connected high-temperature channel between the electrode gap and the cotton disappears. Due to the reduction of energy input, the flame slightly weakens, and the overall temperature shows a downward trend. However, since the cotton has been ignited, the flame gradually intensifies after 4 s and enters the flame development stage. After 8 s, the flame enters the intense combustion stage, and the flame basically completely wraps the cotton. After 16 s, as the cotton gradually burns out, the flame enters the combustion weakening stage and extinguishes after 26 s. It is worth noting that during the combustion weakening stage, although the flame shows a tendency toward extinguishing, the highest temperature of the flame still remains at several thousands of Kelvin until the combustible gas produced by the pyrolysis of the cotton is completely burned out.

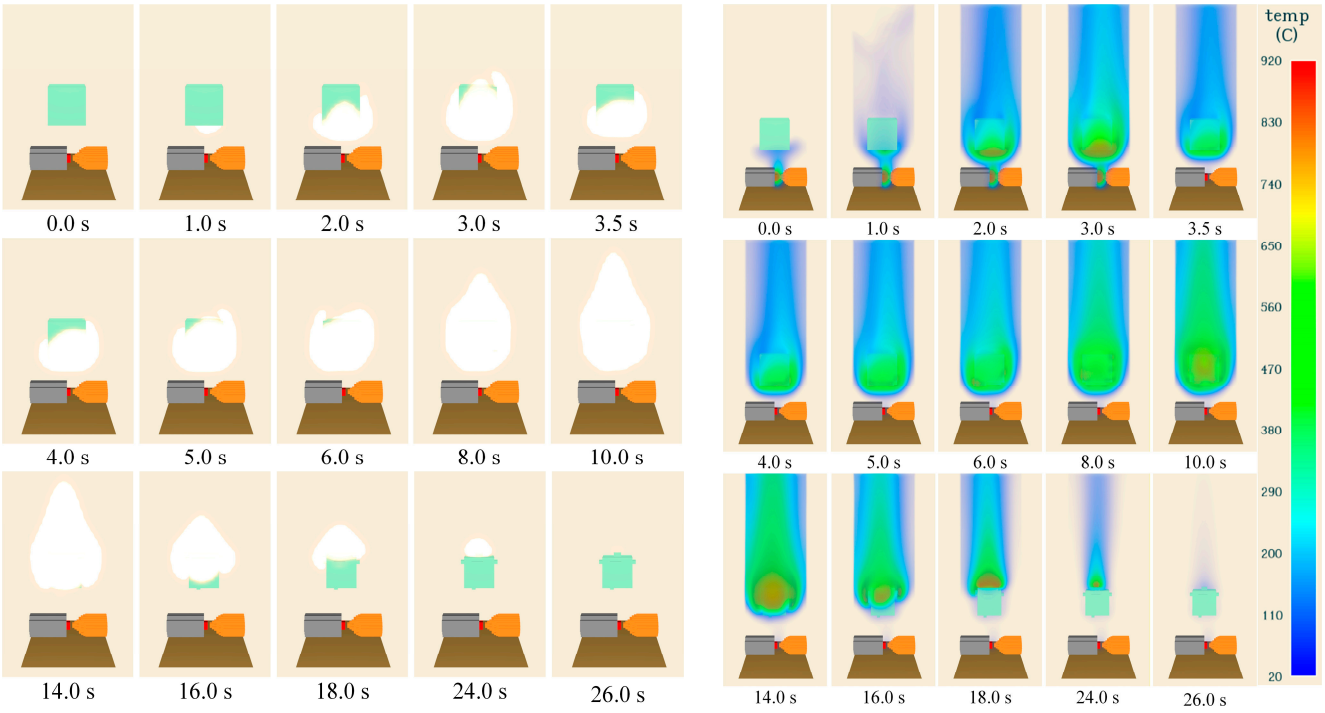


Figure 8. Arc-induced process: (**a**) HRR; (**b**) temperature.

Figure 9 shows the variations in the mass fractions of the pyrolysis gas and combustion product (CO_2). As shown in the figure, during the arc heating stage from 1 to 3 s, due to the high temperature of the arc, the lower surface of the cotton undergoes pyrolysis to produce combustible gas $C_6H_{10}O_5$. At 2 s and 3 s, since the cotton has not been completely ignited, a high concentration of combustible gas accumulates on the lower surface, while the mass fraction of the combustion product CO_2 is relatively low. After 3 s, the arc is cut off, the input energy decreases, the flame weakens, and the mass fraction of the combustible gas produced by pyrolysis decreases, and the mass fraction of CO_2 decreases accordingly. Then, as the flame develops, the mass fraction of the combustible gas gradually increases, and combustible gas is gradually pyrolyzed from the side and top surfaces. At the same time, the combustible gas is ignited, generating combustion heat, further intensifying the flame and increasing the production of CO_2. As the combustible gas is gradually consumed, the flame weakens until it goes out.

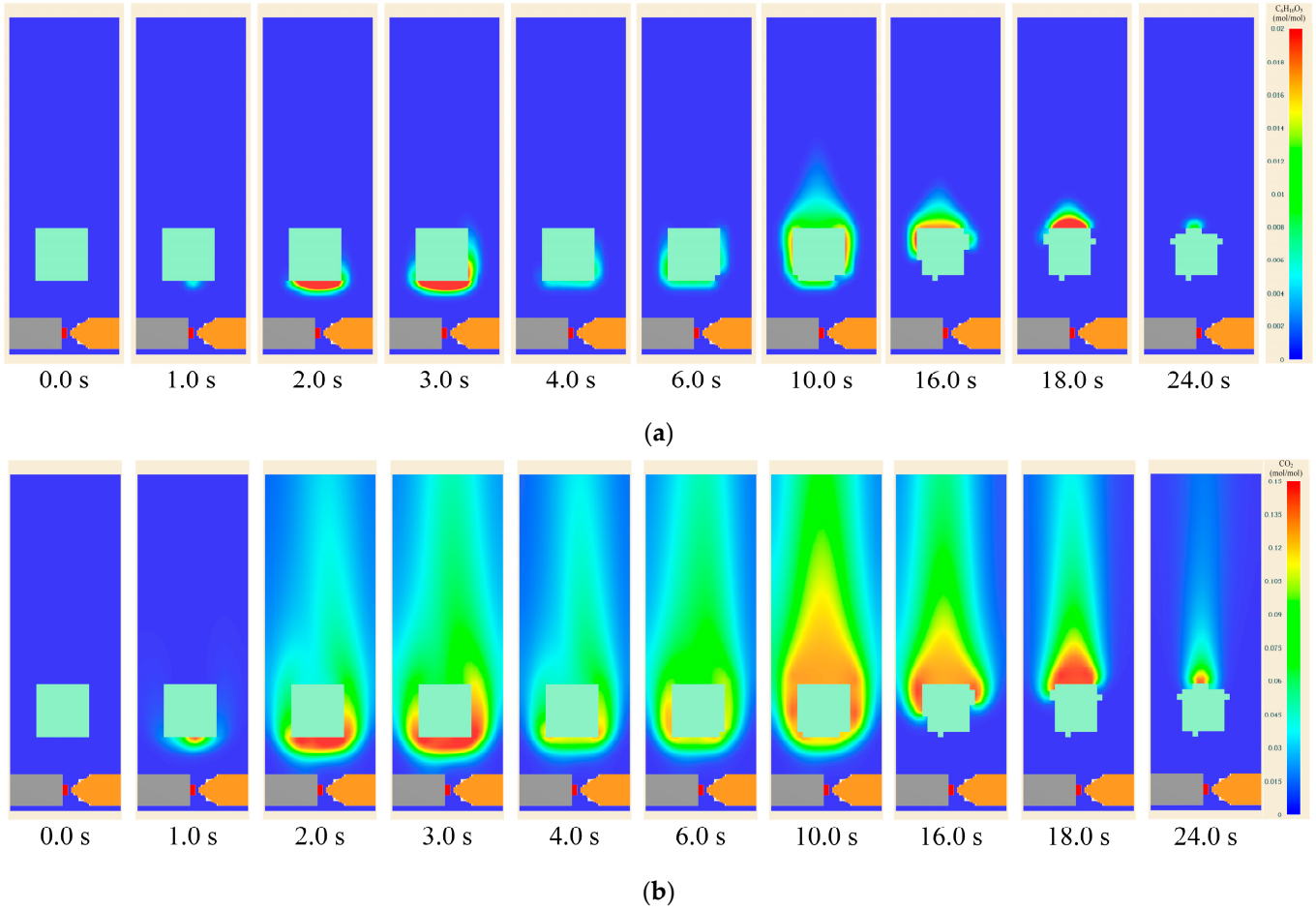


Figure 9. Chemical reaction process: (**a**) $C_6H_{10}O_5$; (**b**) CO_2.

Figure 10 shows the variation curves of the heat release rate (HRR) obtained from the simulation, the temperature variation curves at different heights, the mass fraction of the flammable gas ($C_6H_{10}O_5$), and the mass fraction of the combustion products (CO_2). As shown in the figure, during the period of 0 to 0.6 s, the HRR is basically zero. At this stage, the temperature of the lower surface of the cotton (thermocouple 2) gradually rises to 605 K, which is beyond the ignition point of the cotton. During this period, the mass fractions of $C_6H_{10}O_5$ and CO_2 produced by pyrolysis are relatively low, indicating that the cotton has not yet been ignited, and the input energy is mainly maintained by the arc. During the period of 0.6 to 3 s, the HRR increases rapidly, and the temperatures of the two monitoring points on the lower surface of the cotton (thermocouple 1 and thermocouple 2) also increase rapidly and remain at 1153 to 1473 K, far exceeding the ignition point of the cotton. At this time, the temperatures of the three monitoring points on the upper surface (thermocouple 3, thermocouple 4, and thermocouple 5) rise slowly, remaining below 566 K. During this stage, the mass fractions of the flammable gas and combustion products at the two monitoring points on the lower surface of the cotton increase rapidly. During this period, the heat from the arc and the flame act on the cotton together, accelerating the pyrolysis of the cotton material.

At 3 s, due to the arc being cut off, a rapid decline can be observed in the HRR curve, and the temperature curve, the mass fraction of combustible gas, and the combustion product curve decline accordingly. However, due to thermal inertia and the continued combustion of the combustible gas produced during the arc heating stage, the HRR does not drop to zero and the flame remains burning. After 3.7 s, the HRR curve begins to recover and grow, reaching its peak during the period of 9 to 14 s and maintaining at

around 0.06 to 0.07 kW. Observing the temperature curve, it can be found that after 3.7 s, the curve resumes an upward trend. Around 12 s, the temperatures at the two monitoring points on the lower surface rapidly drop to the ambient temperature of 293 K, while the temperatures at the three monitoring points above the upper surface continue to rise. From the mass fraction curve, the reason can be deduced that the material on the lower surface of the cotton has basically undergone pyrolysis and combustion, and the flame spreads upward along the side of the cotton. After 14 s, the HRR curve begins to decline and drops to zero at around 25 s.

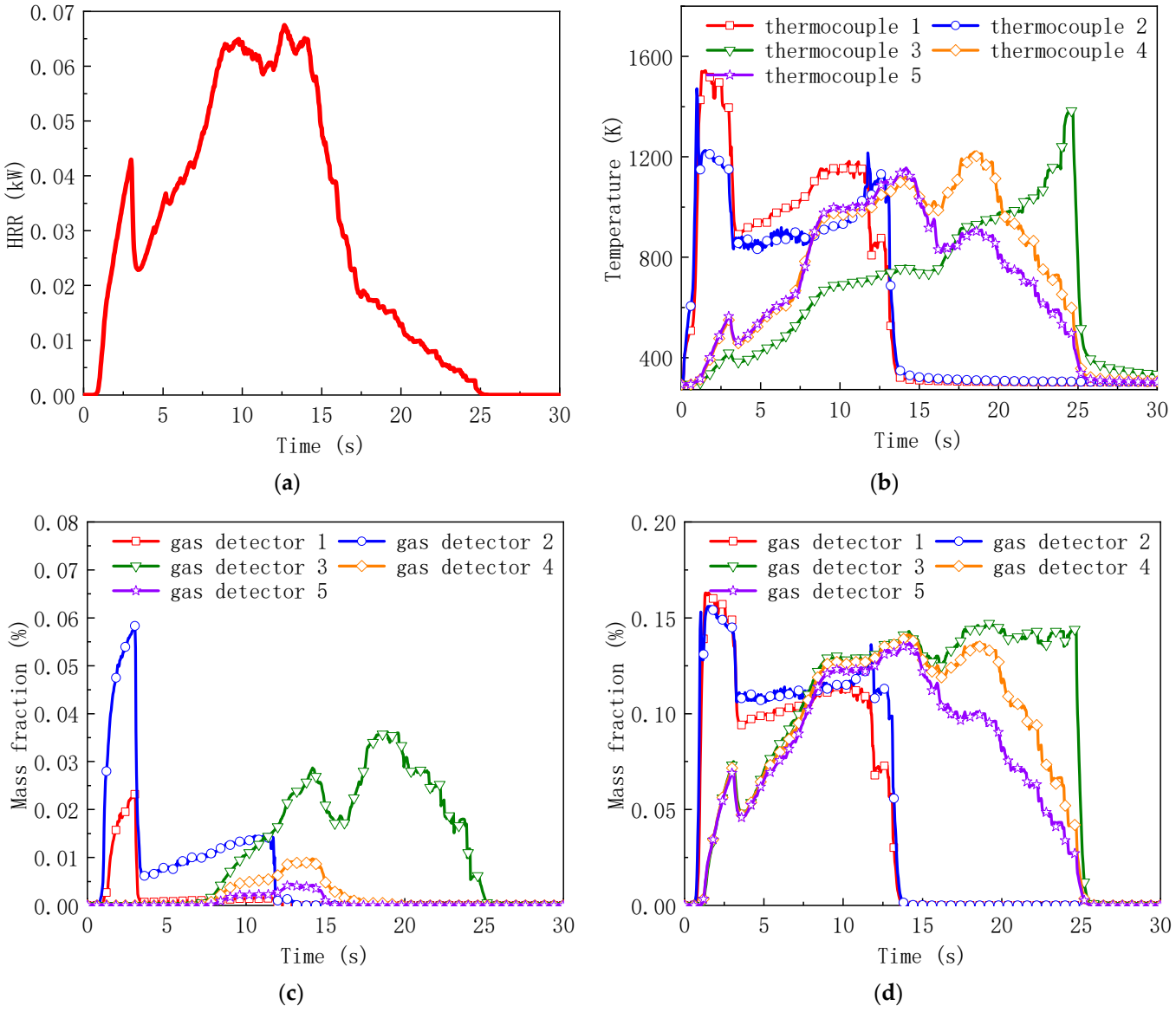


Figure 10. Simulation results: (**a**) HRR; (**b**) temperature; (**c**) mass fraction of $C_6H_{10}O_5$; (**d**) mass fraction of CO_2.

It can be seen from the above simulation images of cotton ignition that ignition initiates at the position closest to the arc heat source (i.e., the lower surface of the cotton in this study). Therefore, the temperature of the cotton's lower surface, the generation characteristics of pyrolysis gas, as well as the combustion products are analyzed hereinafter to explain the ignition mechanism. Figure 11 presents the variations in temperature, pyrolysis gas $C_6H_{10}O_5$, and combustion product CO_2 at monitoring point 2 (the lower surface of the

cotton). To analyze the cotton ignition process, only the curves within 0–5 s are displayed in the figure.

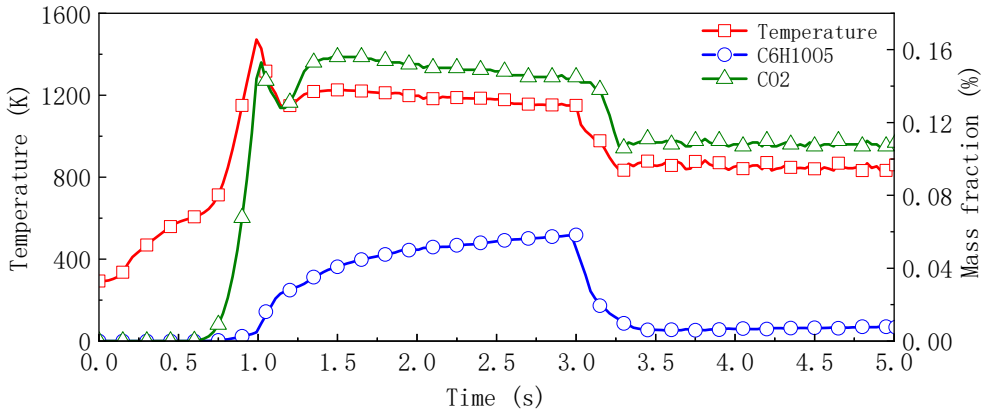


Figure 11. Curves of temperature, pyrolysis gases, and combustion products during the cotton ignition process.

During 0–0.99 s, the temperature of the cotton's lower surface rises continuously under arc heating and exceeds the ignition point of the cotton (423.15–433.15 K) at 0.27 s. However, the mass fractions of both the pyrolysis gas $C_6H_{10}O_5$ and combustion product CO_2 are zero at this moment, indicating that combustibles will not ignite immediately even if the temperature exceeds the ignition point. At 0.63 s, the mass fractions of $C_6H_{10}O_5$ and CO_2 begin to rise from zero, which can be regarded as the ignition time of the cotton. Obviously, the rising rate of $C_6H_{10}O_5$ is lower than that of CO_2, because the amount of $C_6H_{10}O_5$ generated at the initial stage of pyrolysis is small, and most of the $C_6H_{10}O_5$ is combusted to form CO_2 immediately after its generation. Notably, the arc heat is the sole energy source during the period of 0–0.63 s.

At 0.99 s, the temperature presents a sharp peak with a maximum value of 1471 K, followed by a rapid drop. This is due to the heat absorption caused by the ignition of the accumulated $C_6H_{10}O_5$ and the pyrolysis of the cotton at this time, which leads to a temperature decrease near the cotton surface. Although the temperature drops, it remains high enough to induce the pyrolysis of the cotton, so the mass fraction of $C_6H_{10}O_5$ maintains an upward trend. With the heat released by the combustion of $C_6H_{10}O_5$, the temperature of the cotton surface gradually recovers and rises, remaining in the range of 1200–1400 K. At 3 s, the arc is cut off and the external energy input is removed, resulting in a decrease in temperature as well as in the concentrations of pyrolysis gas and combustion product. Nevertheless, the thermal inertia of the cotton itself and the continuous combustion of the accumulated $C_6H_{10}O_5$ prevent the flame from extinguishing, and the combustion mechanism transitions from arc-driven to combustion-driven self-sustenance.

4.4. Influence of Current Levels

As shown in Figures 12 and 13, as the current increases, the peak temperature of the arc rises, and the high-temperature area of the entire temperature field significantly expands. The diameter of the arc column keeps increasing. When the current is 3 A, the highest temperature of the arc reaches 11,500 K. When the current is 30 A, the highest temperature is 22,181 K. With an increase in current, the Joule heat becomes more intense, causing the temperature to rise. At the same time, the arc voltage decreases as the current level increases.

In actual photovoltaic systems, the current levels generated by photovoltaic power generation vary in different seasons, weather conditions, and time periods. Therefore,

the ignition characteristics of arcs under different current levels were analyzed. Figure 14 shows the arc-induced process under different current levels. Figure 15 presents the heat release rate (HRR) and mass loss rate (MLR) of cotton combustion ignited by the DC arc at different current levels (3–30 A). The simulation conditions are as follows: the arc lasts for 3 s, and the cotton is 10 mm away from the center of the electrode gap. Table 1 shows the combustion parameters.

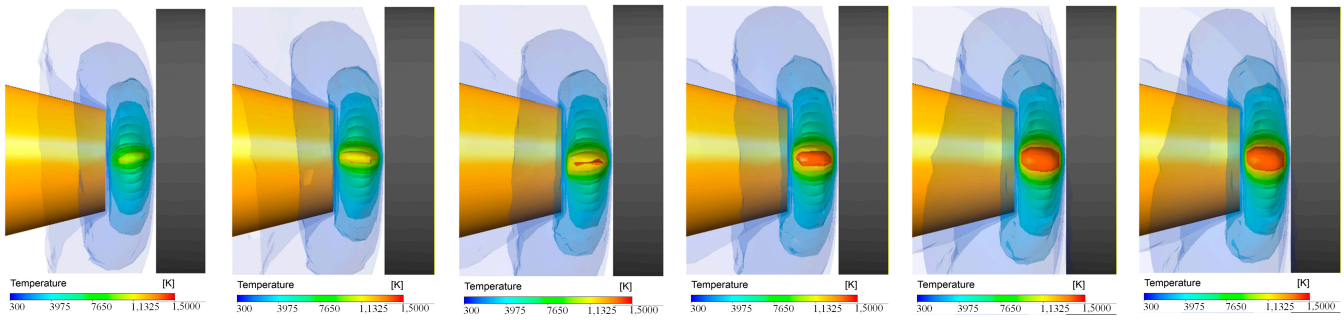


Figure 12. Arc temperatures at different current levels: (**a**) 3 A; (**b**) 8 A; (**c**) 12 A; (**d**) 16 A; (**e**) 24 A; (**f**) 30 A.

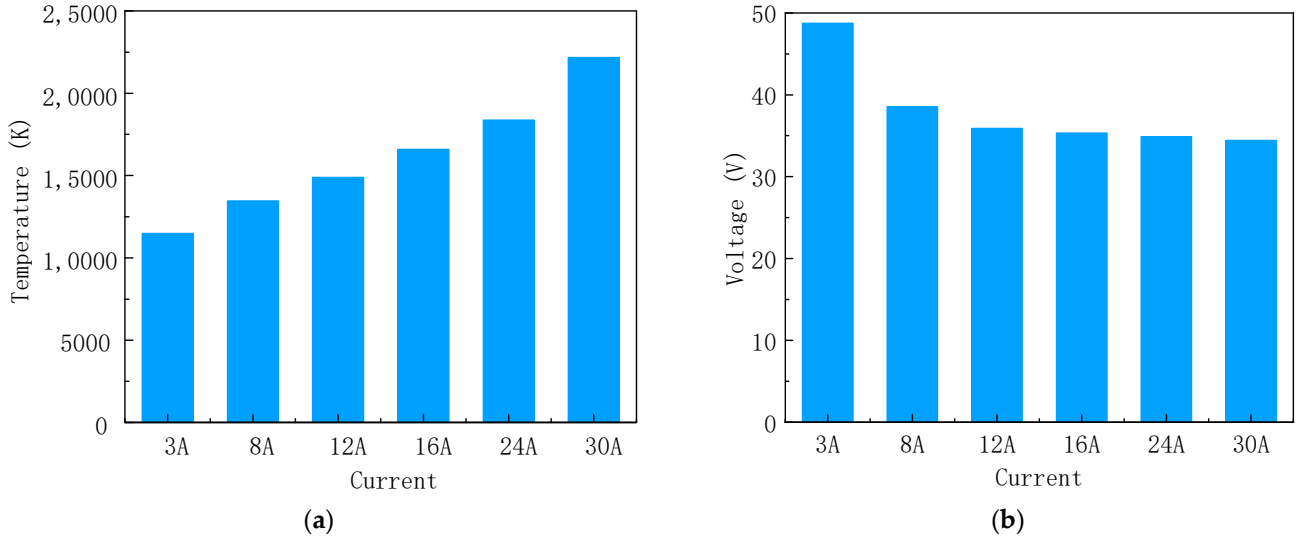


Figure 13. The maximum temperature of the arc and the arc voltage at different current levels: (**a**) maximum temperature; (**b**) arc voltage.

As shown in the figures, under arc conditions of 3 A and 8 A, when the arc is cut off after 3 s, the HRR rapidly drops to zero and the cotton does not continue to burn. However, at currents above 12 A, the cotton can still maintain combustion after the arc is cut off. The HRR and MLR curves at higher current levels are slightly higher than those at lower current levels, but the difference is not significant. As long as the arc power is sufficient to ignite the cotton, after the arc is cut off, the combustion of the cotton is mainly affected by its own properties. It is worth noting that during summer and at midday, when the light is more intense, the risk of fire caused by fault arcs is greater.

Figure 16 shows the variations in temperature and pyrolysis gas $C_6H_{10}O_5$ at monitoring point 2 (i.e., the lower surface of the cotton) within 0–6 s at different current levels. For the 3 A case, the temperature of the cotton's lower surface remains below 372 K before arc extinction, which is lower than the ignition point of the cotton; thus, the arc at 3 A is insufficient to ignite the cotton. For current levels of 8–30 A, a sharp temperature peak

appears in all temperature curves within 0–1.5 ms, and the mechanism underlying the formation of this peak is analyzed in Section 4.3. A higher current level results in greater heat release by the arc, a faster temperature rise rate of the cotton's lower surface, and the temperature peak is reached sooner. After the temperature peak is attained, the temperature drops sharply, which reduces the generation rate of pyrolysis gas. Nevertheless, the high temperature of the arc still sustains the generation and accumulation of pyrolysis gas. Therefore, reaching the temperature peak earlier results in the accumulation of more $C_6H_{10}O_5$ before arc extinction, which provides sufficient fuel for the self-sustaining combustion of the cotton after the arc is cut off. For the 8 A current level, however, the temperature rise rate is relatively low, and the temperature peak is not reached until 2.82 s. Insufficient flammable pyrolysis gas is accumulated before arc extinction; when the arc is cut off at 3 s, the external energy input is lost, and the energy released by the combustion of pyrolysis gas is inadequate to maintain the continuous pyrolysis of the cotton. The flame is extinguished once the generated $C_6H_{10}O_5$ is completely combusted or volatilized.

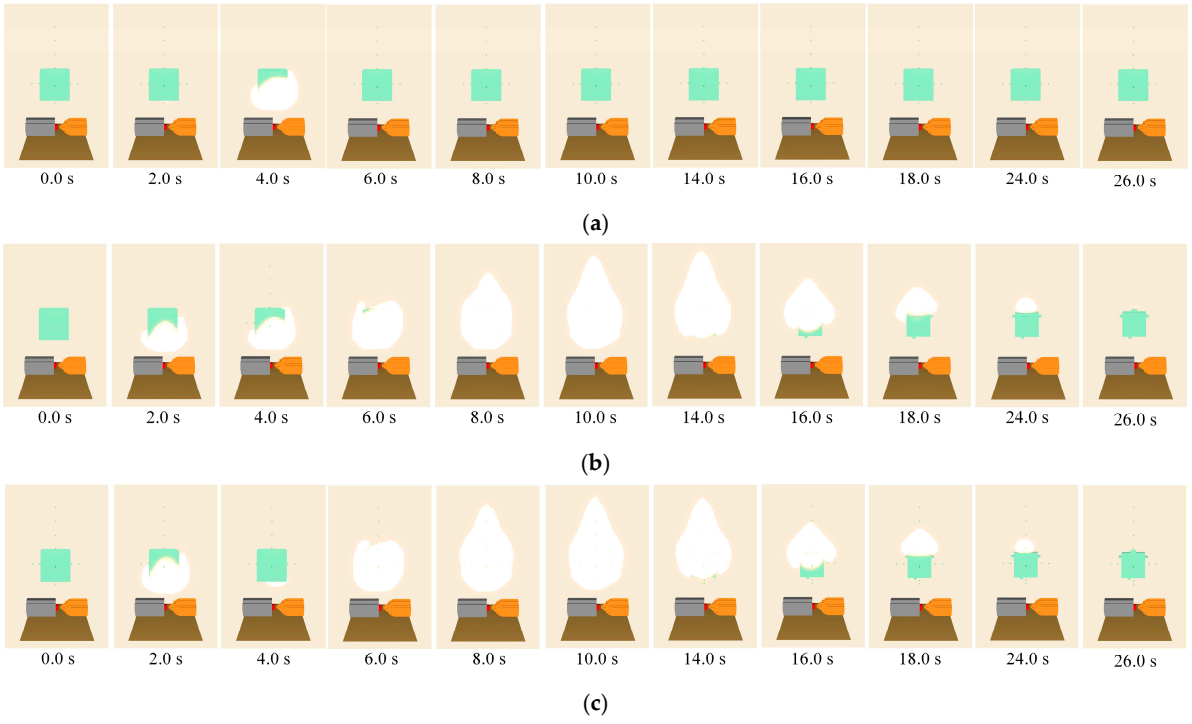


Figure 14. Arc-induced process at different current levels: (**a**) 8 A; (**b**) 16 A; (**c**) 30 A.

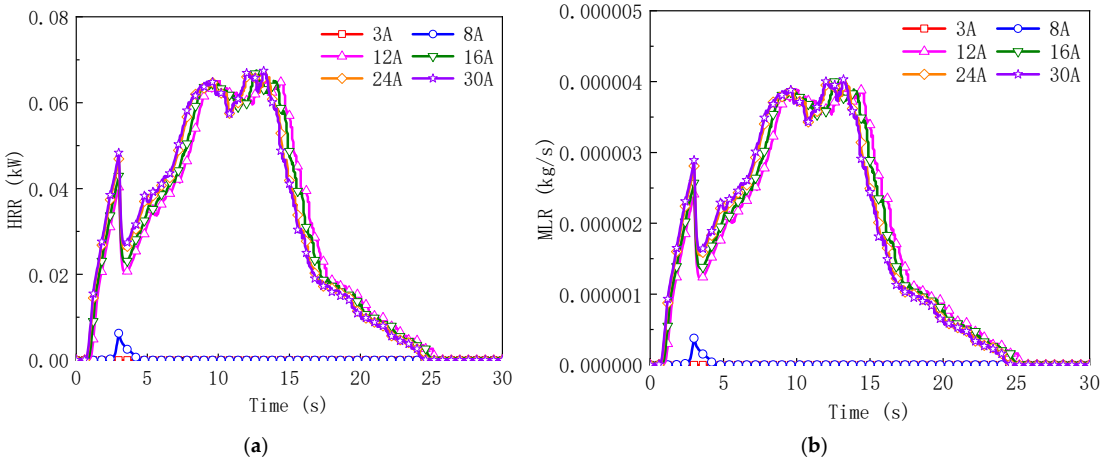


Figure 15. Influence of current level on combustion: (**a**) HRR; (**b**) MLR.

Table 1. Combustion parameters at different current levels.

	3 A	8 A	12 A	16 A	24 A	30 A
Ignition or not	no	yes	yes	yes	yes	yes
Combustion or not	no	no	yes	yes	yes	yes
Temperature peak in arcing duration (K)	-	1395.92	1447.43	1471.34	1491.56	1500.6
$C_6H_{10}O_5$ in arc cutting moment (%)	1.71×10^{-11}	0.02	0.0574	0.0583	0.0594	0.0597
Ignition moment (s)	-	1.62	0.78	0.66	0.54	0.49
Temperature peak moment (s)	-	2.82	1.14	0.99	0.87	0.84
Burning duration (s)	0	4.65	25.6	25.42	25.1	24.6
Max HRR (kW)	6.91×10^{-13}	0.00624	0.0673	0.0675	0.0672	0.0674

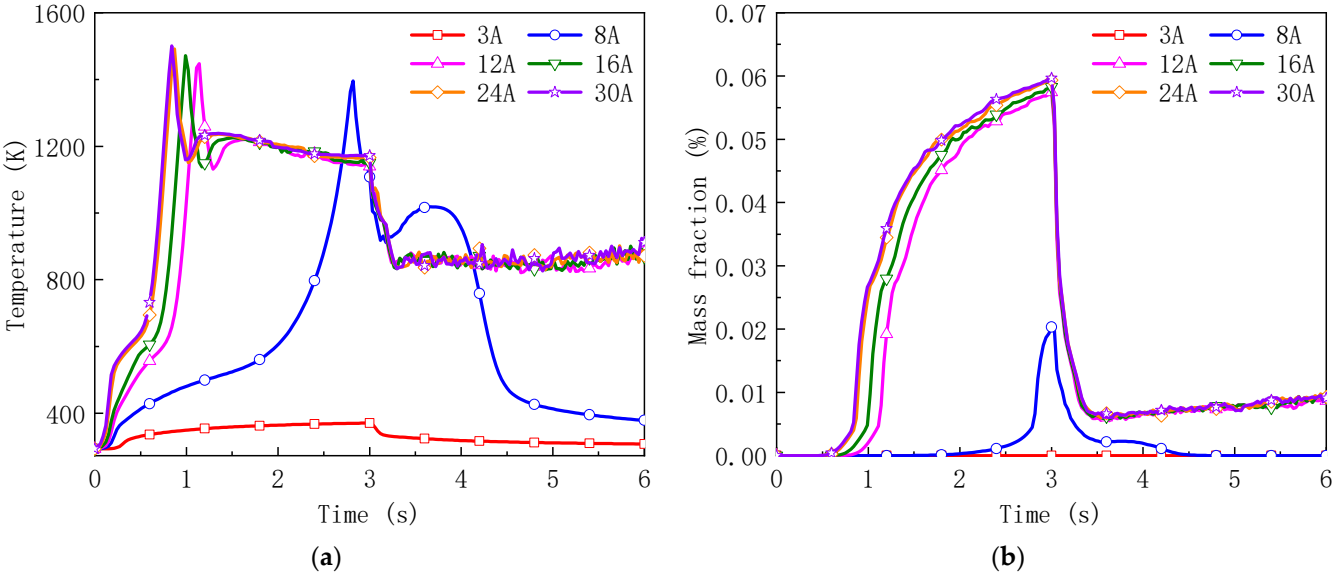


Figure 16. Influence of current levels on temperature and pyrolysis of combustible gases: (**a**) temperature; (**b**) mass fraction of $C_6H_{10}O_5$.

4.5. Influence of Arcing Time

Figure 17 shows the arc-induced process under different arcing times. Figure 18 presents the heat release rate (HRR) and mass loss rate (MLR) of the cotton ignited by a DC arc under different arc durations (1.5–5.0 s). The simulation conditions are as follows: an arc current of 16 A, and the cotton is 10 mm away from the center of the electrode gap. Table 2 shows the combustion parameters.

As shown in the figures, an increase in the arc duration results in a higher HRR at the arc interruption moment, that is, a longer arc duration is more likely to ignite external combustibles. Under an arc duration of 1.5 s, the cotton does not sustain combustion, but it is ignited and sustains combustion under 2.0 s and longer durations. A longer arc duration results in faster growth of the mass loss rate, that is, a faster combustion rate of the cotton. It is worth noting that for DC fault arc circuit breakers (AFDD), the UL1699B standard requires the interruption of the arc fault line within 2.5 s. From the simulation results, for some higher load conditions, there is still a risk of fire within 2.5 s.



Figure 17. Arc-induced process at different arcing times: (**a**) 1.5 s; (**b**) 2.0 s; (**c**) 3.0 s; (**d**) 5.0 s.

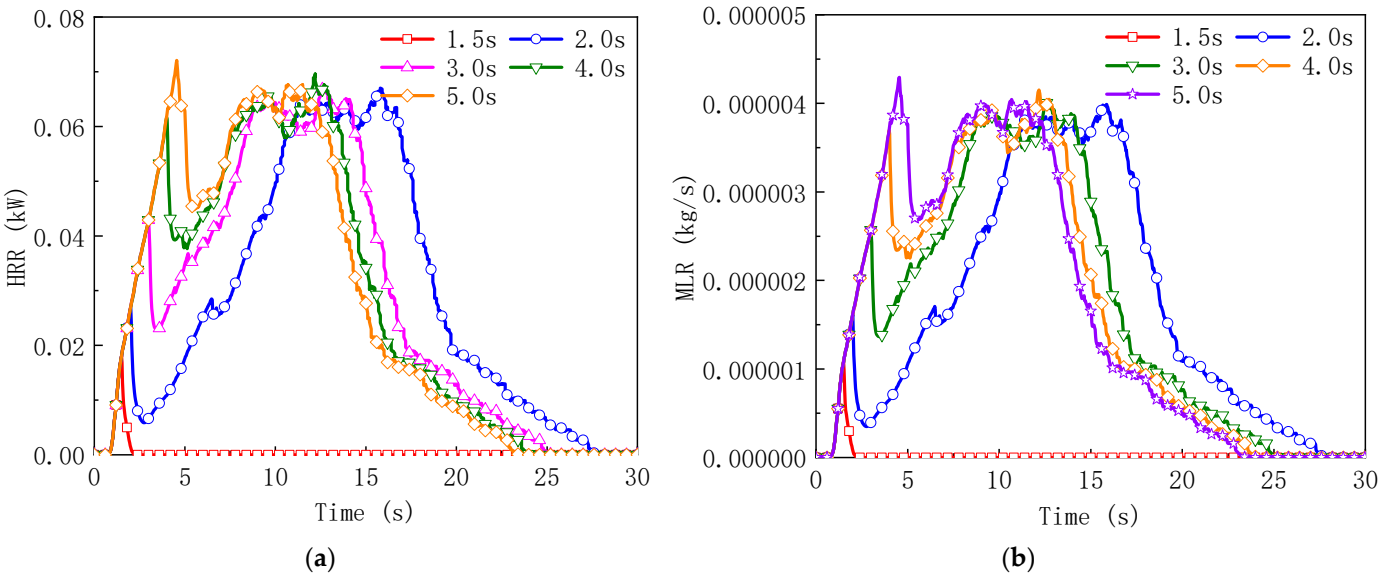


Figure 18. Influence of arcing time on combustion: (**a**) HRR; (**b**) MLR.

Table 2. Combustion parameters at different arcing times.

	1.5 s	2.0 s	3.0 s	4.0 s	5.0 s
Ignition or not	yes	yes	yes	yes	yes
Combustion or not	no	yes	yes	yes	yes
Temperature peak in arcing duration (K)	1471.23	1472.06	1471.34	1471.06	1470.94
$C_6H_{10}O_5$ in arc cutting moment (%)	1.38×10^{-7}	0.0049	0.0583	0.0584	0.0582
Ignition moment (s)	0.66	0.66	0.66	0.66	0.66
Temperature peak moment (s)	0.99	0.99	0.99	0.99	0.99
Burning duration (s)	2.43	28.2	25.7	24.5	23.9
Max HRR (kW)	0.018	0.06699	0.0675	0.0696	0.0721

Figure 19 presents the temperature and mass fraction of pyrolysis gas $C_6H_{10}O_5$ at monitoring point 2 (i.e., the lower surface of the cotton) within 0–6 s at different arcing times. In the initial stage, the temperature of the cotton's lower surface rises continuously under arc heating, with the maximum temperature reaching 1473 K, which is far higher than the ignition point of the cotton. Since the current level is kept constant, the temperature curves and pyrolysis gas mass fraction curves overlap with each other before the arc is cut off. During the arc heating phase, the mass fraction of $C_6H_{10}O_5$ exhibits a steady upward trend. After the arc is cut off, both the temperature and the mass fraction of $C_6H_{10}O_5$ drop sharply. By comparing the mass fraction of $C_6H_{10}O_5$ at the moment of arc interruption, it can be found that a longer arcing duration results in more sufficient $C_6H_{10}O_5$ gas generated by cotton pyrolysis, as shown in Figure 19. After the arc is cut off, the external energy input is lost, and whether the cotton can continue to burn depends on whether the heat released by combustion of the pyrolysis gas is sufficient to maintain the continuous pyrolysis of the remaining solid cotton, thereby continuously supplementing the flammable pyrolysis gas to sustain combustion. Therefore, after arc interruption, the sustainability of combustion depends on the balance between the consumption of existing flammable pyrolysis gas and the generation of new flammable pyrolysis gas. If the generation rate of new flammable gas is lower than its consumption rate, combustion cannot be sustained.

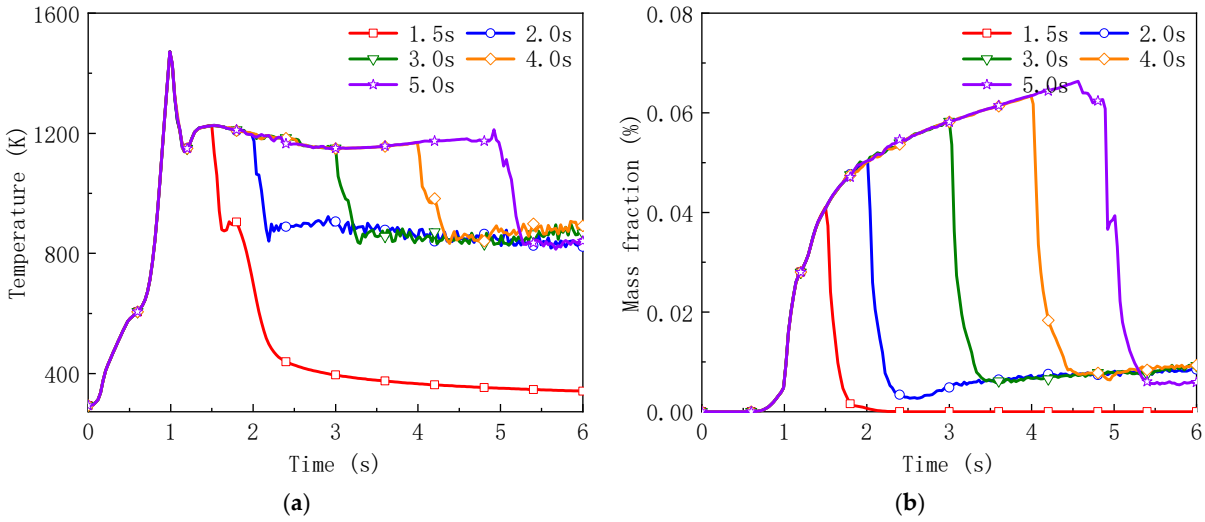


Figure 19. Influence of arcing time on temperature and pyrolysis of combustible gases: (**a**) temperature; (**b**) mass fraction of $C_6H_{10}O_5$.

4.6. Influence of Flammable Material Distance

Figure 20 shows the arc-induced process at different flammable material distances. Figure 21 presents the heat release rate (HRR) and mass loss rate (MLR) of the cotton ignited by a DC arc at different distances between the combustible material and the arc. The simulation conditions are as follows: an arc current of 16 A, and an arc duration of 3 s. Table 3 shows the combustion parameters.

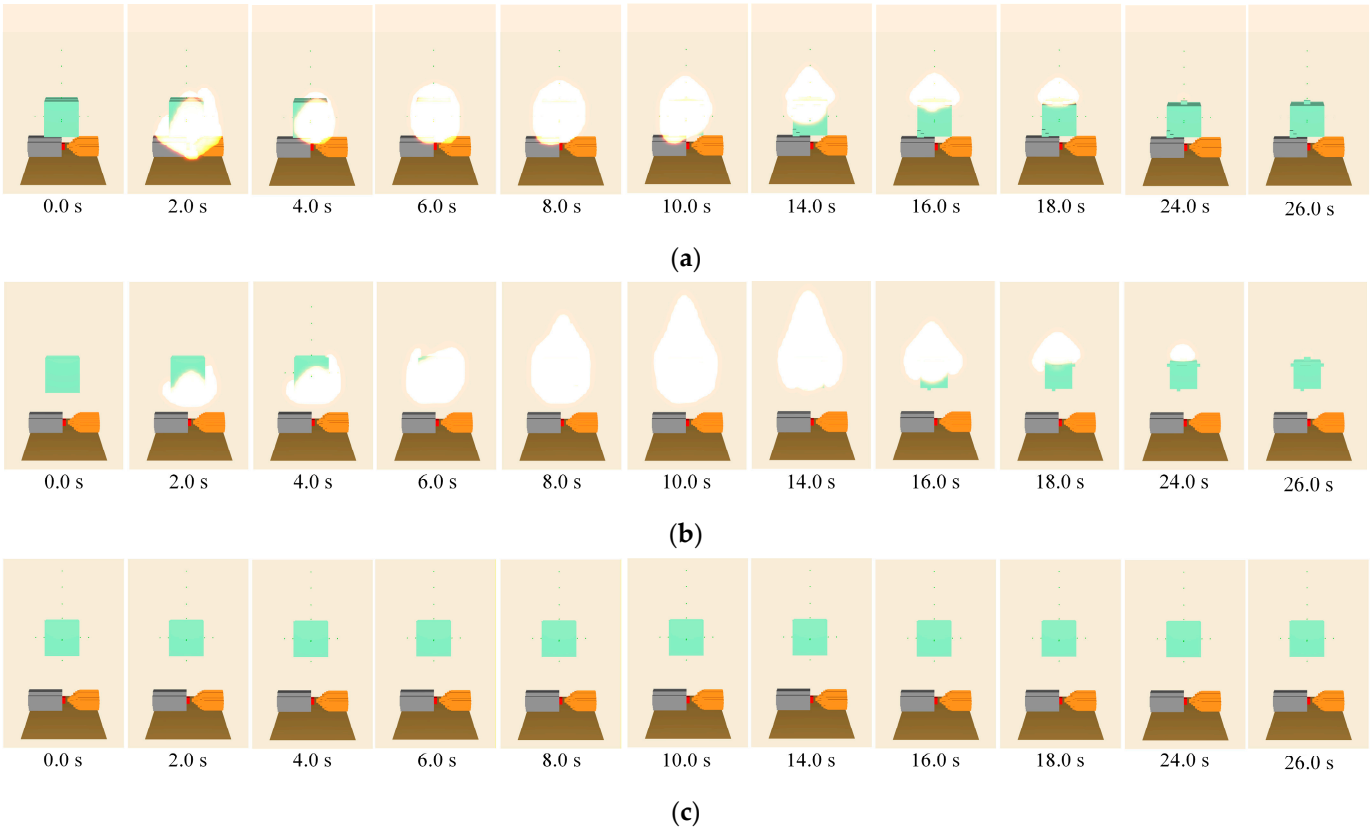


Figure 20. Arc-induced process at different flammable material distances: (**a**) 4.0 mm; (**b**) 10.0 mm; (**c**) 14.0 mm.

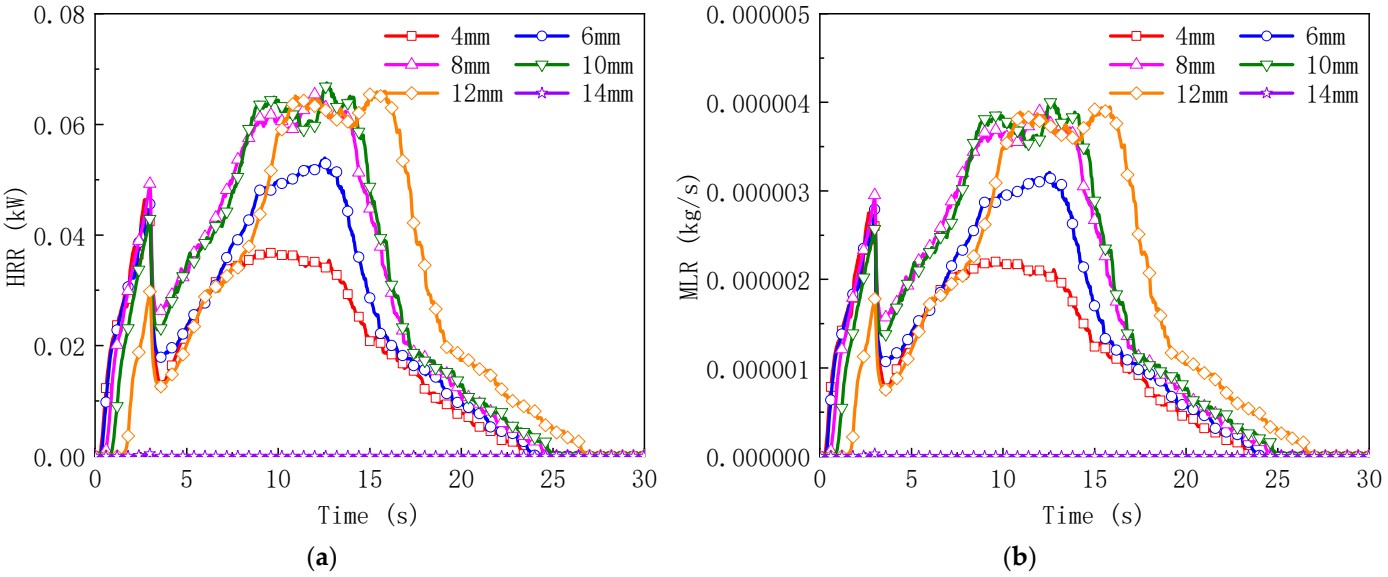


Figure 21. Influence of flammable material distance on combustion: (**a**) HRR; (**b**) MLR.

Table 3. Combustion parameters at different flammable material distances.

	4.0 mm	6.0 mm	8.0 mm	10.0 mm	12.0 mm	14.0 mm
Ignition or not	yes	yes	yes	yes	yes	no
Combustion or not	yes	yes	yes	yes	yes	no
Temperature peak in arcing duration (K)	1762.07	1701.44	1551.75	1471.34	1366.35	547.582
$C_6H_{10}O_5$ in arc cutting moment (%)	0.1698	0.1663	0.0863	0.0583	0.0412	8×10^{-5}
Ignition moment (s)	0.24	0.3	0.47	0.66	1.08	-
Temperature peak moment (s)	0.33	0.39	0.63	0.99	1.8	-
Burning duration (s)	23.9	24.5	25	25.7	27.5	0
Max HRR (kW)	0.0464	0.0539	0.0654	0.0675	0.066	0.00047

As shown in the figure, when the distance is 14 mm, the cotton is not ignited. At other distances, the cotton is ignited. A shorter distance results in faster cotton ignition, a higher HRR during the arc heating stage, and a shorter time for the cotton to burn out. Therefore, in actual circuits, the wiring should be reasonably arranged, and flammable materials should be avoided around circuits.

Figure 22 shows the temperature, pyrolysis gas $C_6H_{10}O_5$, and combustion product CO_2 at monitoring point 2 (i.e., the lower surface of cotton) within 0–6 s for different distances between the cotton and the arc. A shorter distance between the cotton and the arc results in a faster temperature rise rate of the cotton's lower surface and a higher peak temperature, leading to a greater yield and a higher generation rate of pyrolysis gas $C_6H_{10}O_5$. The ignition performance degrades with increasing distance, which is attributed to the attenuation of arc heat transfer. The heat transferred from the arc to the combustible is mainly realized through thermal radiation and convection, and the heat attenuation of the arc intensifies as the distance increases. A shorter distance results in faster ignition and a higher heat release rate because a higher heat flux density shortens the energy accumulation time of the cotton and promotes the rapid generation and combustion of the pyrolysis gas. Notably, for the 4 mm distance case, the pyrolysis gas exhibits a trend of first decreasing and then increasing in the time intervals of 1.59–1.89 s and 2.13–2.52 s, and the combustion product simultaneously shows a convex peak phenomenon. The same phenomenon is also observed in the 6 mm distance case. This is because a closer distance results in more intense combustion; when the pyrolysis gas accumulates to a certain amount on the surface, the combustion is intensified, thus consuming pyrolysis gas and oxygen rapidly and in large quantities. The reduction in surrounding oxygen, in turn, slows down the combustion intensity, allowing the amount of pyrolysis gas to recover gradually. Therefore, it can be inferred that a closer distance results in greater fluctuations in combustion.

4.7. Influence of Copper Vapor

During the development of the arc, high temperatures may cause the melting and evaporation of the electrode material, thereby leading to electrode wear and changes in the physical properties of the arc medium. This section analyzes the influence of the metal vapor concentration on electrode ablation.

Assume that the gas in the arc region is a mixture of air and copper vapor, with the concentration of copper vapor increasing from 0% to 20%. Figure 23 shows arc temperature cloud diagrams of different metal vapor concentrations at 16 A and 1 mm. Figure 24 shows the maximum arc temperature and arc voltage. As the concentration of metal vapor

increases, the temperature of the arc column generally shows a downward trend, and the arc column gradually shrinks. Generally speaking, the electrical conductivity of the mixed gas increases with an increase in the metal vapor concentration. The increase in electrical conductivity leads to a reduction in Joule heat, and when the thermal conductivity remains unchanged, it causes the arc temperature to decrease. At the same time, the decrease in pressure drop produced by the same current density results in a decrease in arc voltage.

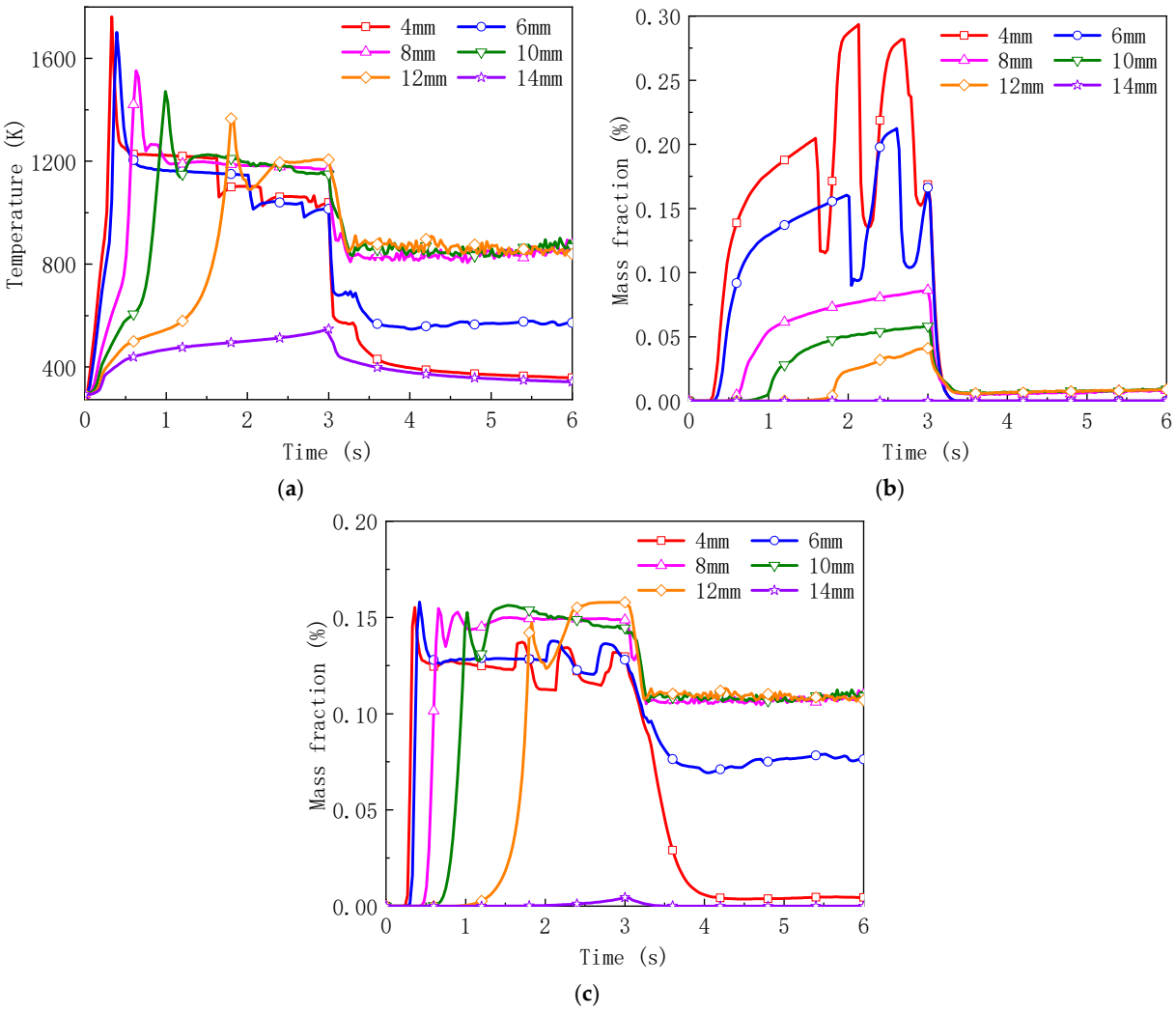


Figure 22. Influence of flammable material distance on temperature and pyrolysis of combustible gases: (**a**) temperature; (**b**) mass fraction of $C_6H_{10}O_5$; (**c**) mass fraction of CO_2.

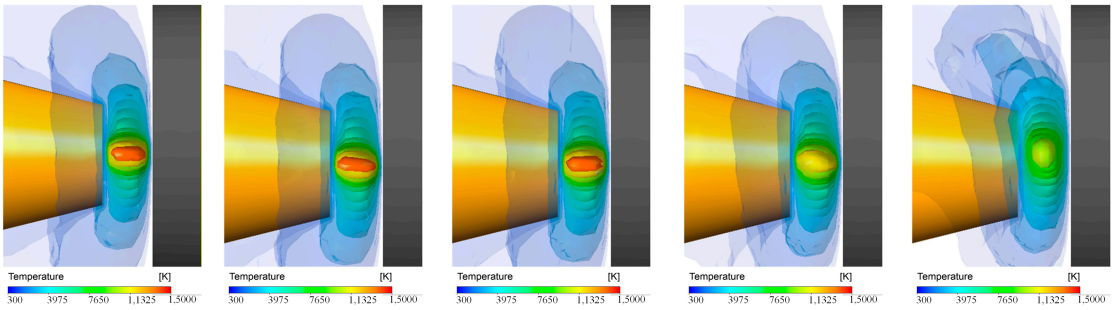


Figure 23. Arc temperatures at different copper vapor concentrations: (**a**) 0%; (**b**) 0.1%; (**c**) 1%; (**d**) 10%; (**e**) 20%.

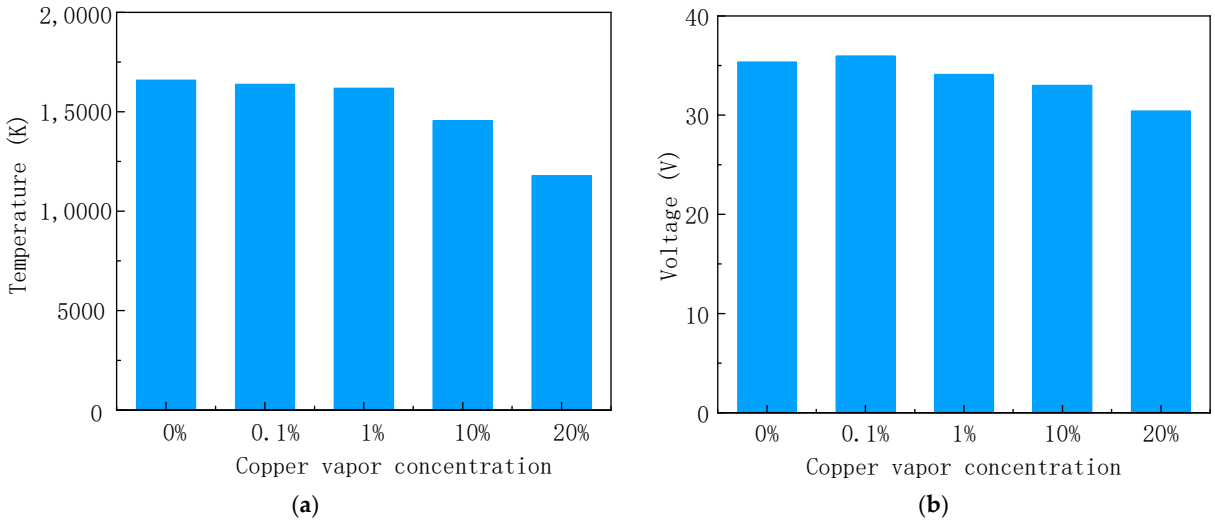


Figure 24. The maximum temperature of the arc and the arc voltage at different copper vapor concentrations: (**a**) maximum temperature; (**b**) arc voltage.

Figure 25 illustrates the combustion of the cotton at different copper vapor concentrations. Figure 26 presents the heat release rate (HRR) and mass loss rate (MLR) of cotton ignition by the direct current arc when exposed to different copper vapor concentrations. The simulation conditions are as follows: a direct current of 16 A, an arc duration of 3 s, and the distance between the cotton and the center of the electrode gap is 10 mm. Table 4 shows the combustion parameters.



Figure 25. Arc-induced process at different copper vapor concentrations: (**a**) 0%; (**b**) 1%; (**c**) 10%; (**d**) 20%.

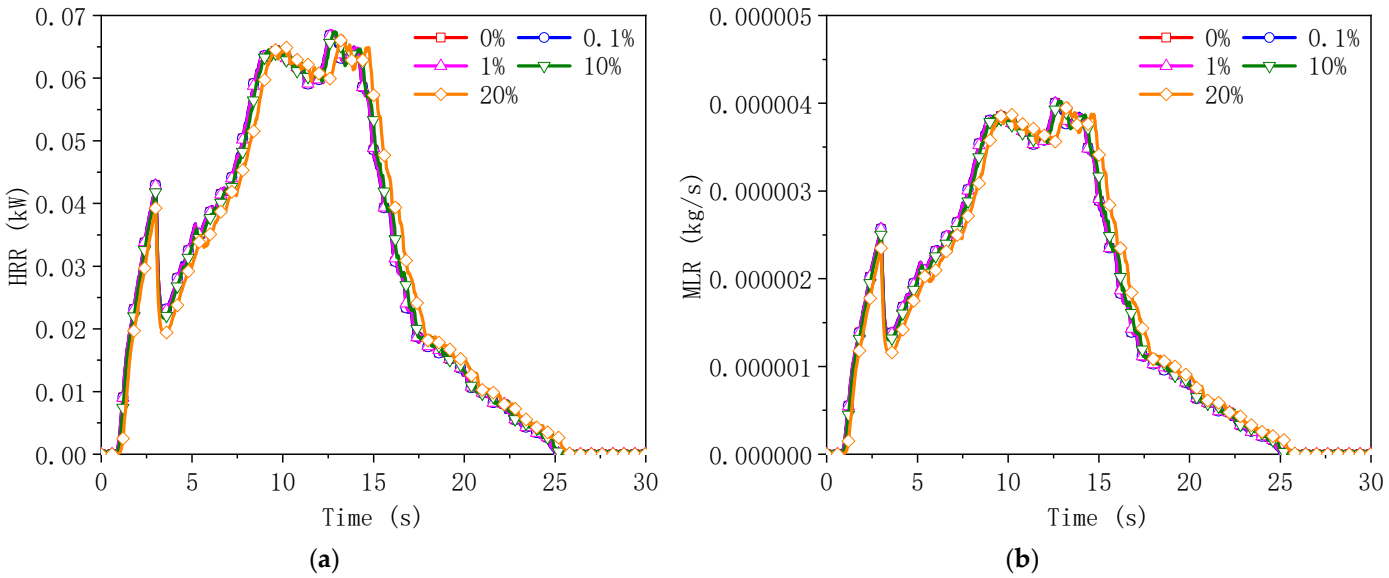


Figure 26. Influence of copper vapor concentration on combustion: (**a**) HRR; (**b**) MLR.

Table 4. Combustion parameters at different copper vapor concentrations.

	0%	**0.1%**	**1%**	**10%**	**20%**
Ignition or not	yes	yes	yes	yes	yes
Combustion or not	yes	yes	yes	yes	yes
Temperature peak in arcing duration (K)	1471.34	1471.34	1470.78	1465.46	1458.08
$C_6H_{10}O_5$ in arc cutting moment (%)	0.0232	0.0232	0.0232	0.023	0.0227
Ignition moment (s)	0.66	0.66	0.66	0.72	0.84
Temperature peak moment (s)	0.99	0.99	0.99	1.05	1.2
Burning duration (s)	25.7	25.7	25.74	25.92	26.37
Max HRR (kW)	0.0675	0.0675	0.0675	0.0674	0.0667

As shown in Figures 25 and 26, under the action of a direct current arc with a copper vapor concentration ranging from 0% to 20%, the cotton is all ignited. From the HRR and MLR curves, it can be seen that the curves at copper vapor concentrations of 0% to 1% basically overlap. However, the ignition time and combustion time at a 20% copper vapor concentration are slightly longer than those at lower copper vapor concentrations. This is because at high copper vapor concentrations, the temperature of the arc is relatively low but still sufficient to reach the ignition point of the cotton. Based on the above analysis of the arc, it can be concluded that metal vapor has a significant influence on the temperature distribution of the arc column, but it does not have a significant impact on the ignition of external combustible materials by the arc.

Under actual working conditions, the interaction between the electric arc and the electrode is extremely complex. Besides generating metal vapor, it can also cause material transfer, complex heat and mass transfer, etc. Moreover, distribution of the metal vapor is generally uneven. Therefore, this analysis was conducted under relatively idealized conditions. Further in-depth studies under actual complex working conditions will be carried out in subsequent research.

Figure 27 shows the temperature and pyrolysis gas $C_6H_{10}O_5$ at monitoring point 2 (i.e., the lower surface of cotton) at different activation energies. A higher content of copper vapor in the arc medium results in a lower temperature rise rate, a longer ignition time of cotton, and a lower generation rate of pyrolysis gas. As analyzed above, an increase in the content of metal vapor in the arc medium leads to a decreasing trend in arc temperature, which weakens the heat source and further reduces the pyrolysis rate. Its influence mechanism on combustion is similar to that discussed in Section 4.4.

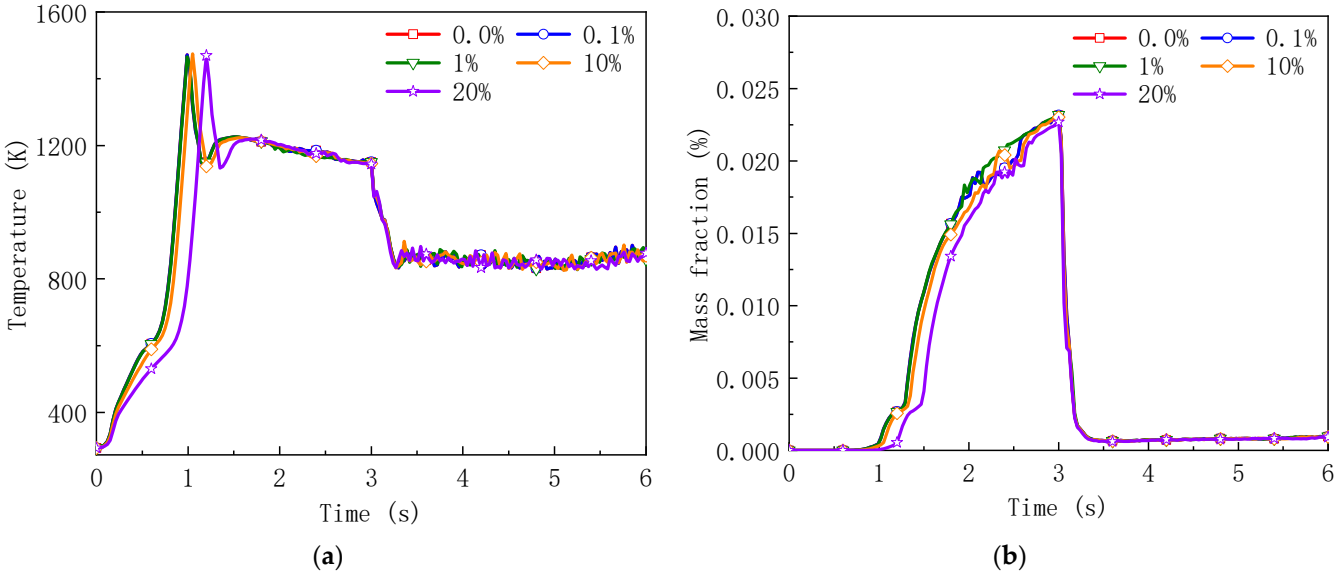


Figure 27. Influence of copper vapor on temperature and pyrolysis of combustible gases: (**a**) temperature; (**b**) mass fraction of $C_6H_{10}O_5$.

4.8. Influence of Pyrolytic Parameter

According to ref. [35], the activation energy for untreated cotton is 148.77 kJ/mol, the activation energy for cotton treated with zinc diacetate is 125.17 kJ/mol, and the activation energy for cotton treated with zinc benzoate is 132.51 kJ/mol. In the above text, the activation energy of 148.77 kJ/mol for untreated cotton given by ref. [35] is used in the simulation analysis. This section analyzes the cotton ignition conditions at different activation energies. Table 5 shows the combustion parameters.

Table 5. Combustion parameters at different pyrolytic parameters.

	125.17 kJ/mol	**132.5 kJ/mol**	**148.74 kJ/mol**
Ignition or not	yes	yes	yes
Combustion or not	yes	yes	yes
Temperature peak in arcing duration (K)	1470.32	1464.99	1471.34
$C_6H_{10}O_5$ in arc cutting moment (%)	0.0438	0.0375	0.0232
Ignition moment (s)	0.49	0.54	0.66
Temperature peak moment (s)	0.65	0.75	0.99
Burning duration (s)	27.39	>30	25.7
Max HRR (kW)	0.147	0.1186	0.0675

Figure 28 illustrates the combustion of cotton at activation energies of 125.17 kJ/mol, 132.51 kJ/mol, and 148.74 kJ/mol. Figure 29 presents the heat release rate (HRR) and mass loss rate (MLR) of cotton ignition by the direct current arc when ignited at different activation energies (125.17 kJ/mol, 132.51 kJ/mol, and 148.74 kJ/mol). The simulation conditions are as follows: a direct current of 16 A, an arc duration of 3 s, and the distance between the cotton and the center of the electrode gap is 10 mm.

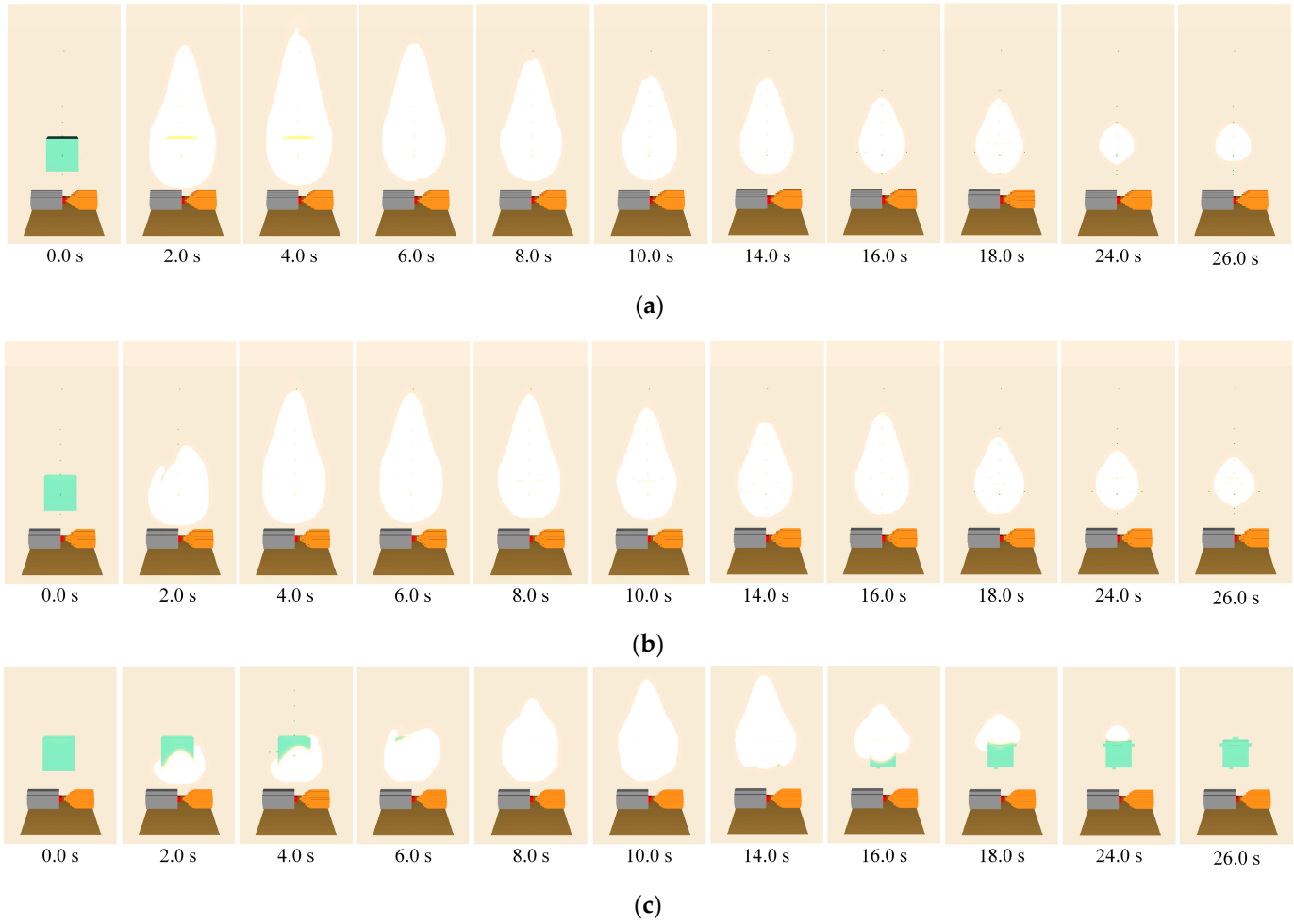


Figure 28. Arc-induced process at different pyrolytic parameters: (**a**) 125.17 kJ/mol; (**b**) 132.51 kJ/mol; (**c**) 148.74 kJ/mol.

From Figure 29, it can be seen that at an activation energy of 125.17 kJ/mol, the combustion of cotton is the most intense, with the highest flame height, and the flame completely envelops the cotton by 2.0 s. The second highest combustion intensity of the cotton occurs at an activation energy of 132.51 kJ/mol. At 26 s, the cotton continues to burn in both cases of 125.17 kJ/mol and 132.51 kJ/mol. However, the combustion intensity is the lowest at an activation energy of 148.74 kJ/mol.

Figure 30 presents the temperature and pyrolysis gas $C_6H_{10}O_5$ at monitoring point 2 (i.e., the lower surface of cotton) within 0–6 s at different activation energies. A lower activation energy results in a faster temperature rises, the temperature peak is attained sooner, and a higher generation rate of $C_6H_{10}O_5$. It can be observed that the combustion intensity is enhanced with a decrease in the activation energy. According to Arrhenius reaction kinetics [36], a lower activation energy means less energy is required to initiate the pyrolysis reaction of cotton. Consequently, the pyrolysis rate is faster under the same arc heat input, releasing more flammable volatiles in a short time, which drives the

rapid development of the flame and an increase in the heat release rate. The higher flame height and longer combustion duration at lower activation energies are attributed to the continuous and rapid pyrolysis of the cotton matrix, which supplies a stable fuel source for the combustion reaction.

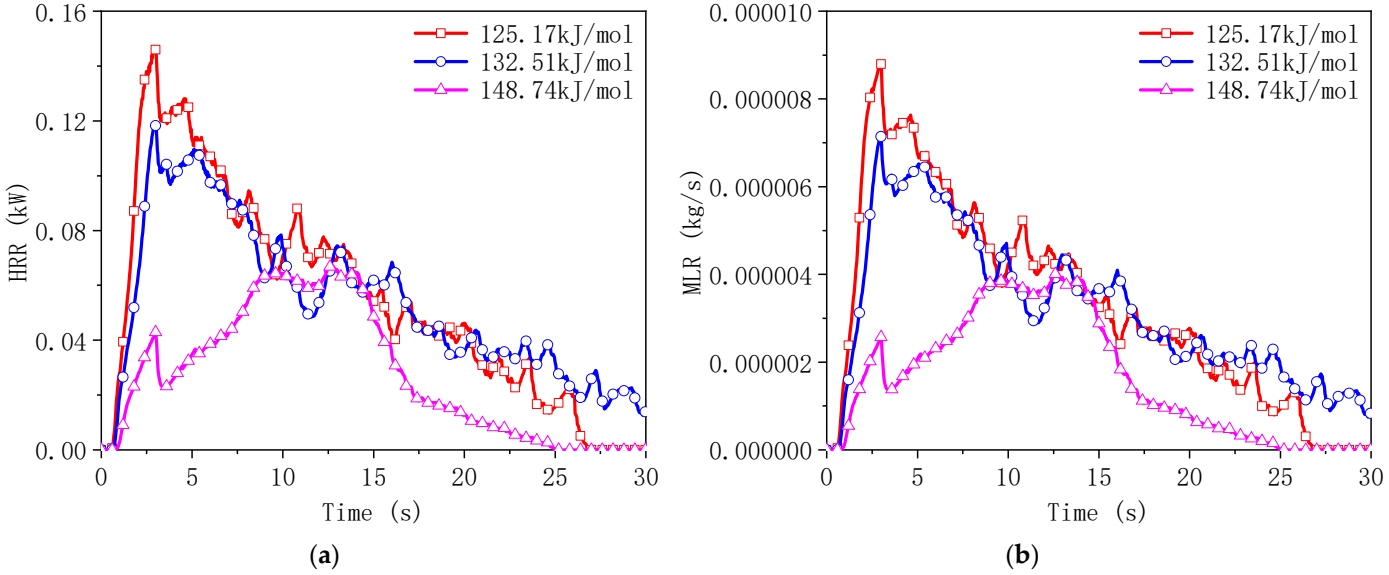


Figure 29. Influence of pyrolytic parameter on combustion: (**a**) HRR; (**b**) MLR.

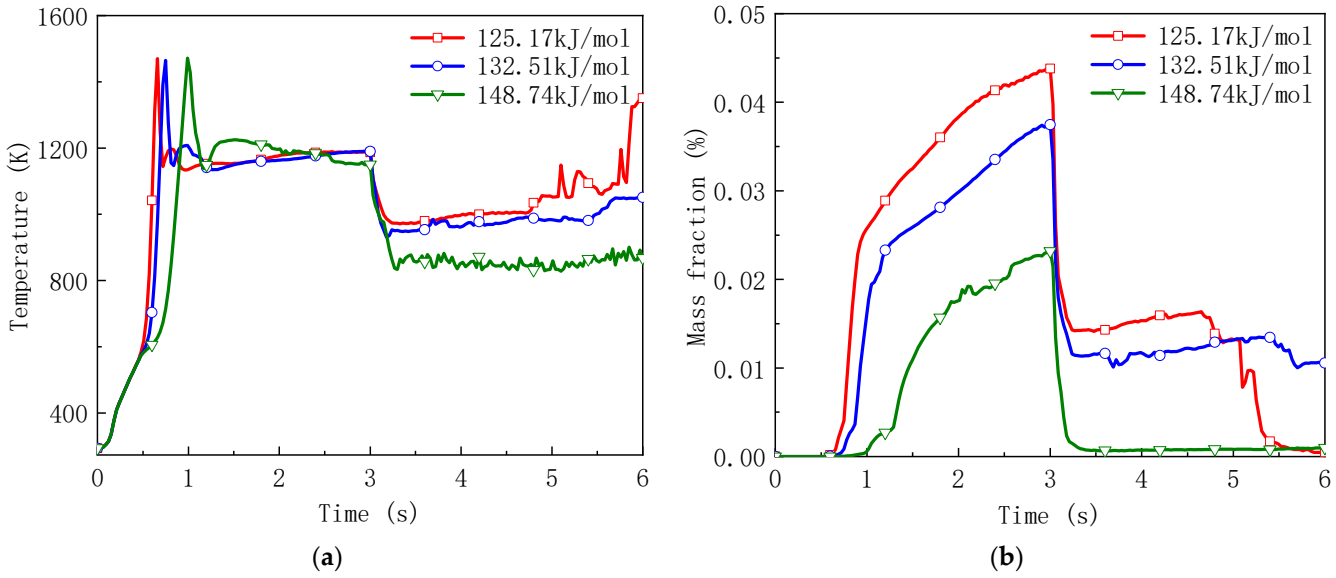


Figure 30. Influence of pyrolytic parameter on temperature and pyrolysis of combustible gases: (**a**) temperature; (**b**) mass fraction of $C_6H_{10}O_5$.

5. Conclusions

This paper combines the magnetohydrodynamic (MHD) theory and energy balance theory to establish a three-dimensional numerical model of a DC fault arc in a photovoltaic system, simulates the entire process from the combustion to the extinction of the DC fault arc, and verifies the validity of the simulation model through experimental data. On this basis, combined with the combustion reaction model of the complex pyrolysis model, a simulation model of a fault arc igniting external combustibles is established, revealing the heat transfer, mass transfer, chemical reactions, and other mechanisms of a DC fault arc

igniting external combustibles, and the arc ignition risk is analyzed under factors such as current level, arc burning time, and distance of combustibles.

The key findings are summarized below:

1. The current level is a key factor influencing the ignition ability of DC fault arcs. The peak temperature of the arc and the range of the high-temperature area significantly increase with an increase in current. After the 3 A and 8 A arcs are cut off, combustible materials cannot continue to burn. Arcs with a current of 12 A or above can achieve the continuous ignition of combustible materials. Moreover, under the high-current conditions of photovoltaic systems during the summer and midday, with strong light periods, the risk of arc fires is significantly increased.
2. The arc duration directly determines the ignition effect of combustible materials. An arc duration of 1.5 s is insufficient to sustain the continuous combustion of cotton fibers. An arc duration of 2.0 s or longer can achieve stable ignition, and a longer arc duration results in a higher HRR at the time of arc interruption and a faster rate of mass loss of the combustible material. The 2.5 s arc interruption time required by the UL1699B standard still poses a fire ignition risk under some high-load photovoltaic system operating conditions.
3. The distance between the combustible material and the arc has a significant impact on the ignition process. When the distance between the combustible material and the center of the arc is 14 mm, ignition does not occur. However, when this distance is less than 14 mm, ignition can be achieved. A shorter distance results in faster ignition of combustible material, a higher HRR during the arc heating stage, and a shorter burnout time. Reasonable planning of the line layout and keeping lines away from combustible material can effectively reduce the risk of arc ignition.
4. The concentration of copper vapor will alter the physical properties of the electric arc. As the copper vapor concentration increases from 0% to 20%, the temperature of the arc column shows a downward trend, the volume shrinks, and the arc voltage also decreases. However, since the arc temperature can still reach the ignition point of combustible materials, the overall effect of the copper vapor concentration on the ignition of external combustible materials is not significant. It only slightly prolongs the ignition and combustion time of combustible materials at high concentrations.
5. The activation energy of the thermal decomposition of combustibles directly affects the intensity of combustion. A lower activation energy results in more vigorous combustion of combustibles. Zinc acetate-treated cotton (125.17 kJ/mol) ignites faster and has a higher flame height than zinc benzoate-treated cotton (132.51 kJ/mol) and untreated cotton (148.74 kJ/mol). Moreover, combustibles with lower activation energies have a longer combustion duration after being ignited by an electric arc. The thermal decomposition characteristics of the combustible are an important internal factor for the development of combustion after it is ignited by an electric arc.

In this paper, modeling of the electric arc is based on the assumption of local thermodynamic equilibrium, and the coupling effect of electrode melting is not taken into account in the simulation. Moreover, the single-step global reaction and centralized substance combustion model adopted in the combustion model are simplifications of the actual phenomenon. A more comprehensive model will be constructed and verified in subsequent research.

Author Contributions: Conceptualization and methodology, R.S., P.Z. and Y.X.; validation, R.S., P.Z. and W.W.; original draft preparation, Y.X. and W.W.; writing—original draft preparation, R.S.; writing—review and editing, R.S., P.Z. and W.W. All authors have read and agreed to the published version of the manuscript.

Funding: This work was supported by State Grid Technology Project of the research and application of key technologies for the measurement and diagnosis of the low voltage arc fault considering various types of power sources, load, time, and spatial factors (Project No. 5700-202455276A-1-1-ZN).

Data Availability Statement: The original contributions presented in this study are included in the article. Further inquiries can be directed to the corresponding author.

Conflicts of Interest: Authors Runan Song, Penghe Zhang and Yang Xue were employed by the company China Electric Power Research Institute. The remaining authors declare that the research was conducted in the absence of any commercial or financial relationships that could be construed as a potential conflict of interest.

References

1. Ferraz, R.G.; Iurinic, L.U.; Filomena, A.D.; Gazzana, D.S.; Bretas, A.S. Arc Fault Location: A Nonlinear Time Varying Fault Model and Frequency Domain Parameter Estimation Approach. *Int. J. Electr. Power Energy Syst.* **2016**, *80*, 347–355. [CrossRef]
2. Qu, N.; Wang, J.; Liu, J. An Arc Fault Detection Method Based on Current Amplitude Spectrum and Sparse Representation. *IEEE Trans. Instrum. Meas.* **2019**, *68*, 3785–3792. [CrossRef]
3. Huang, X.; Wu, C.; Li, Z.; Wang, F. Comparative Study of DC Arc Fault Detection Methods in Photovoltaic Systems. *Acta Energiae Solaris Sin.* **2020**, *41*, 204–214.
4. Shekhar, A.; Ramirez-Elizondo, L.; Bandyopadhyay, S. Detection of Series Arcs Using Load Side Voltage Drop for Protection of Low Voltage DC Systems. *IEEE Trans. Smart Grid* **2018**, *9*, 6288–6297. [CrossRef]
5. *UL 1699*; Standard for Arc-Fault Circuit-Interrupters. UL Standards: Northbrook, IL, USA, 2017.
6. *GB/T 3143-1982*; Liquid Chemical Products—Color Determination (Hazen Unit—Platinum-Cobalt Scale). National Bureau of Standards: Beijing, China, 1982.
7. Du, L.; Xu, Z.; Chen, D. Improved Control Strategy for Carbonized Cable Preparation in Low-voltage Arc Fault Test. *Chin. J. Electr. Eng.* **2023**, *4*, 122–131. [CrossRef]
8. Huang, J.; Xu, Z.; Du, L. Method for Reconstructing Arc Fault Current Signals and An Adaptive Correction Strategy. *Chin. J. Electr. Eng.* **2024**, *4*, 129–140. [CrossRef]
9. Miller, D.B.; Hildenbrand, J.L. DC Arc Model Including Circuit Constraints. *IEEE Trans. Power Appar. Syst.* **1973**, *PAS-92*, 1926–1934. [CrossRef]
10. Nottingham, W.B. A New Equation for The Static Characteristic of The Normal Electric Arc. *Am. Inst. Electr. Eng.* **1923**, *42*, 302–310. [CrossRef]
11. Cassie, A.M. A New Theory of Rupture and Circuit Severity. *CIGRE Rep.* **1939**, *102*, 2–14.
12. Mayr, O. Beitrage zur Theorie des Statischen und Des Dynamischen Lichtbogens. *Arch. Elektrotech.* **1943**, *37*, 588–608. [CrossRef]
13. He, J.; Wang, K.; Li, J. Application of An Improved Mayr-type Arc Model in Pyro-breakers Utilized in Superconducting Fusion Facilities. *Energies* **2021**, *14*, 4383. [CrossRef]
14. Wang, Y.; Liu, Y.; Ning, X. Research on The Randomness of Low-Voltage AC Series Arc Faults Based on The Improved Cassie Model. *Energies* **2025**, *18*, 538. [CrossRef]
15. Wang, Q.; Ge, S.; Cao, W. Study of Arc Interruption Characteristics under Rated Current in Low Voltage Circuit Breakers. *Energies* **2023**, *16*, 4114. [CrossRef]
16. Wang, W.; Li, Z.; Gao, K. Dynamic Characteristics of Transverse-Magnetic-Field Induced Arc for Plasma-Jet-Triggered Protective Gas Switch in Hybrid UHVDC System. *Energies* **2022**, *15*, 5871. [CrossRef]
17. Ali, K.; Niayesh, K. Effects of Fast Elongation on Switching Arcs Characteristics in Fast Air Switches. *Energies* **2020**, *13*, 4846. [CrossRef]
18. Bo, K.; Zhou, X.; Zhai, G. Simulation of Arc Dwelling Behavior During Bridge-Type Contacts Opening Process for High-Power Relay. *IEEE Trans. Compon. Packag. Manuf. Technol.* **2018**, *8*, 975–981. [CrossRef]
19. Ren, Z.; Nemoto, Y.; Suzuki, Y. Analysis of Adverse Influence of Metal Vapor to Arc Movement Between Electrodes with External Magnetic Field Applied by Numerical Simulation. *IEEJ Trans. Electr. Electron. Eng.* **2022**, *17*, 183–193. [CrossRef]
20. Huang, K.; Sun, H.; Niu, C. Simulation of Arcs for DC Relay Considering Different Impacts. *Plasma Sci. Technol.* **2020**, *22*, 21–30. [CrossRef]
21. Liu, X.; Huang, X.; Cao, Q. Simulation and Experimental Analysis of DC Arc Characteristics in Different Gas Conditions. *IEEE Trans. Plasma Sci.* **2021**, *49*, 1062–1071. [CrossRef]
22. Shin, Y.J.; Woo, J.Y. Effects of Welding Time and Electrical Power on Thermal Characteristics of Welding Spatter for Fire Risk Analysis. *Energies* **2020**, *13*, 6502. [CrossRef]

23. Lu, F.; Wang, H.; Murphy, A. Analysis of Energy Flow in Gas Metal Arc Welding Processes Through Self-consistent Three-dimensional Process Simulation. *Int. J. Heat Mass Transf.* **2014**, *68*, 215–223. [CrossRef]
24. Wang, X.; Zhang, Q.; Liu, Y. Impact of Welding Current on Arc Physical Characteristics in Single-power, Double-wire, Single-arc Gas Metal Arc Welding. *Weld. World* **2025**, *69*, 2657–2668. [CrossRef]
25. Jiang, F.; Peng, S.; Zhang, G. Investigation of Arc Behavior and Welding Formation for A Novel Vector Gas Regulated Plasma Arc Welding. *J. Manuf. Process.* **2024**, *119*, 768–780. [CrossRef]
26. Anthony, M.; Thomas, D. Prediction of Arc, Weld Pool and Weld Properties with A Desktop Computer Model of Metal-inert-gas Welding. *Weld. World* **2017**, *61*, 623–633.
27. Xie, Z.; Hou, L.; He, P. Research on The Fire Risk of Photovoltaic DC Fault Arcs Based on Multiphysical Field Simulation. *Energies* **2025**, *18*, 1396. [CrossRef]
28. Zhou, L.; Wei, W.; Zeng, Z. Thermal Behavior of Electrodes and Ignition Characteristics of Printer Paper Induced by AC Arc Faults. *Case Stud. Therm. Eng.* **2025**, *71*, 106210. [CrossRef]
29. Zhang, J.; Su, G.; Chen, T. Glowing Contact in Electrical Fires: Experimental Investigation and Modeling on Its Heat Intensity and Thermal Hazards. *Case Stud. Therm. Eng.* **2023**, *45*, 102880. [CrossRef]
30. Zhang, X.; Reda, I.; Aram, M. Wind-driven Smoke Dispersion in Rooftop Photovoltaic Fires: An Experimental Investigation with Helium Smoke. *J. Build. Eng.* **2024**, *83*, 108467. [CrossRef]
31. Courty, L.; Garo, J.P. External Heating of Electric Cables: Numerical Simulation and Auto-ignition Investigation. *J. Hazard. Mater.* **2017**, *321*, 528–536. [CrossRef] [PubMed]
32. Gong, T.; Xie, Q.; Huang, X. Fire Behaviors of Flame-retardant Cables Part I: Decomposition, Swelling and Spontaneous Ignition. *Fire Saf. J.* **2018**, *95*, 113–121. [CrossRef]
33. Wu, Q.; Zhang, R.; Tu, R. Simulation Study on Steady-State Heat Transfer Characteristics of DC Arc Fault. *Trans. China Electrotech. Soc.* **2021**, *36*, 2697–2709.
34. Yang, F.; Tang, Z.; Shen, Y. Parameter Determination Method of Cassie-Mayr Hybrid Arc Model Based on Magnetohydrodynamics Plasma Theory. *Front. Energy Res.* **2022**, *10*, 808289. [CrossRef]
35. Wang, J.; Wang, X.; Song, L.; Hu, Y. Mildew and Pyrolysis Behavior of Cotton Treated with Two Organic Zinc Complexes. *Fire Saf. Sci.* **2019**, *28*, 211–221.
36. Tang, Z.; Xu, Z.; Ye, X. Experimental and Numerical Investigation of Cable Carbonization Under AC Fault Arc. *Proc. CSEE* **2024**, *44*, 9496–9506.

Disclaimer/Publisher's Note: The statements, opinions and data contained in all publications are solely those of the individual author(s) and contributor(s) and not of MDPI and/or the editor(s). MDPI and/or the editor(s) disclaim responsibility for any injury to people or property resulting from any ideas, methods, instructions or products referred to in the content.